Ocean Engineering 281 (2023) 114892

Contents lists available at ScienceDirect

Ocean Engineering

journal homepage: www.elsevier.com/locate/oceaneng

Deriving spatial wave data from a network of buoys and ships

Raphaël E.G. Mounet [a,b,*], Jiaxin Chen [c], Ulrik D. Nielsen [a,b], Astrid H. Brodtkorb [b], Ajit C. Pillai [c], Ian G.C. Ashton [c], Edward C.C. Steele [d]

[a] DTU Construct, Technical University of Denmark, Kgs. Lyngby, DK-2800, Denmark
[b] Centre for Autonomous Marine Operations and Systems (NTNU AMOS), Department of Marine Technology, Norwegian Univ. of Science and Technology, Trondheim, NO-7052, Norway
[c] Renewable Energy Group, Department of Engineering, Faculty of Environment, Science, and Economy, University of Exeter, Penryn, TR10 9FE, UK
[d] Met Office, FitzRoy Road, Exeter, Devon, EX1 3PB, UK

ARTICLE INFO

Keywords:
Sea state estimation
Spectral wave model
Ship motions
Wave-buoy analogy
Machine learning
Metocean conditions

ABSTRACT

The real-time provision of high-quality estimates of the ocean wave parameters at appropriate spatial resolutions are essential for the sustainable operations of marine structures. Machine learning affords considerable opportunity for providing additional value from sensor networks, fusing metocean data collected by various platforms. Exploiting the ship-as-a-wave-buoy concept, this article proposes the integration of vessel-based observations into a wave-nowcasting framework. Surrogate models are trained using a high-fidelity physics-based nearshore wave model to learn the spatial correlations between grid points within a computational domain. The performance of these different models are evaluated in a case study to assess how well wave parameters estimated through the spectral analysis of ship motions can perform as inputs to the surrogate system, to replace or complement traditional wave buoy measurements. The benchmark study identifies the advantages and limitations inherent in the methodology incorporating ship-based wave estimates to improve the reliability and availability of regional sea state information.

1. Introduction

1.1. Motivation

Ocean wave conditions affect human activities, both near the coasts and at sea. Conducting these activities requires broad access to reliable wave datasets (e.g. hindcast, nowcast, and forecast), which form a fundamental basis of the meteorological and oceanographic (metocean) characterisation of these environments (and associated hazards). In particular, this information is crucial for the safe and energy-efficient design, construction, and operation of marine assets. Among the many applications of high-resolution regional wave datasets, assessments of the wave environment are made in connection with initial resource assessments for marine renewable energy harvesting systems, as well as for the planning of installation, inspection, operation, and maintenance of nearshore and offshore infrastructures. Furthermore, the spatial and temporal variability of sea state conditions considerably impacts ship operations, including those of offshore service vessels. 'Go/no-go' decision-making requires accurate spatial wave information from shore to site to guarantee the safety of the crew, ship, and equipment throughout the operation window, while keeping the financial cost of weather delays to a minimum. Consequently, it is essential to achieve a reliable characterisation of the sea state, either from high-resolution statistical descriptions, e.g. long-term hourly hindcast databases of the wave variables, or from short- to medium-term forecast strategies, in which the metocean data are expected to be available on a daily basis and provided within a timely manner (typically just minutes or hours after their production) (Alvarez Fanjul et al., 2022).

Modelling the local and regional wave environment often relies on the support of third-generation, physics-based wave models, such as WAM (WAve Modelling) (Günther et al., 1992; Komen et al., 1996), WAVEWATCH-III (Tolman et al., 2002, 2009), or Simulating Waves Nearshore (SWAN) (Booij et al., 1999; Ris et al., 1999). Over the years, the performance of nearshore models has progressed enormously in terms of resolution refinement (e.g. through downscaling), parameterisation of physical processes (e.g. model source terms for wave growth and dissipation), and spatial extents. However, the increasingly sophisticated mathematical formulations – involving coupled nonlinear partial differential equations (PDEs) to simulate physical processes with high fidelity – tend to increase the dimensions of the computational scheme and, consequently, increase the computational time. Moreover, modern models are highly sensitive to the quality of the input wind

* Corresponding author at: DTU Construct, Technical University of Denmark, Kgs. Lyngby, DK-2800, Denmark.
E-mail address: regmo@dtu.dk (R.E.G. Mounet).

https://doi.org/10.1016/j.oceaneng.2023.114892
Received 21 February 2023; Received in revised form 10 May 2023; Accepted 20 May 2023
Available online 8 June 2023

fields, seen as the dominant forcing process for wave generation, with the application of wind data from different reanalysis datasets affecting the accuracy of results obtained (Lavidas et al., 2017). Meteorological institutes have improved the quality of their wave estimations and predictions by calibrating and validating physics-based models (as well as post-processing their outputs), through the assimilation of global-scale remotely sensed data from satellites and aircraft, complemented with in-situ measurements from wave buoys. The latter are known to be excellent instruments for measuring sea state parameters (Krogstad et al., 1999). Yet, the scarcity of offshore buoys, as most are deployed in nearshore areas, and the high cost of remote sensing systems, in addition to the sparse temporal and geographical coverage from such instruments, pose an additional technical constraint in the assembly of high-quality hindcast and forecast products.

In recent years, with the rapid development of artificial intelligence (AI) applications, research has increasingly considered ways to integrate AI algorithms into traditional physics-based models (Browne et al., 2007; James et al., 2018; Chen et al., 2021, 2022). Surrogate models for spatial wave hindcasting/forecasting have shown promising results in capturing the spatial patterns derived by physics-based models, providing spatial wave information in good agreement with the physics-based model outputs, while using significantly less computational power. James et al. (2018) generated a SWAN-based machine learning framework in which the same inputs as the numerical model were used to estimate the spatial wave height and period by training a multi-layer perceptron model. Their surrogate model showed good agreement with the numerical model and with a five-thousand-fold improvement in computational speed. More recently, Chen et al. (2021) proposed a machine-learning framework in which a random forest algorithm successfully learned the nonlinear correlations between fixed points and spatially distributed wave data across a region using a physics-based model (SWAN). In that case, the surrogate model demonstrated mostly equivalent accuracy for nowcasts when compared to leading numerical models, but run using wave buoy data at a fraction of the computational cost. The work by Chen et al. (2021) showed significant potential for the wider integration of metocean sensors to improve the accuracy and availability of wave data for marine applications.

With this in mind, and given the sheer number of vessels in transit across the oceans, the ship-as-a-wave-buoy concept is appealing as a mature technology for ship response-based sea state estimation (SSE) (Iseki and Ohtsu, 2000; Pascoal and Guedes Soares, 2009; Nielsen, 2006, 2017; Brodtkorb et al., 2018a,b; Chen et al., 2020; Zago et al., 2023). The underlying idea of the so-called *wave-buoy analogy* (WBA) consists of the onboard processing of measurements of the wave-induced responses from a ship in order to facilitate a real-time identification of the sea state at the ship's location. The motions of modern vessels are typically monitored by sensors, therefore constituting a dataset which can potentially be used in real-time in a fundamentally similar way to traditional wave rider buoys, albeit with several further challenges (e.g. due to the more complicated hydrodynamics of a ship). Following the extensive research efforts conducted over the last two decades, various model-based WBA methods (Tannuri et al., 2003; Nielsen and Stredulinsky, 2012; Brodtkorb and Nielsen, 2022) have been validated, as well as for machine learning-based approaches — a rigorous comparison of which was made by Mittendorf et al. (2022) in terms of accuracy, robustness and computational cost. Combined with data from the more conventional observation platforms, ship-based measurements could be the input to a networked procedure to estimate – with greater confidence – the wave systems encountered. Research was recently initiated in this direction (Nielsen et al., 2019; Mounet et al., 2022), considering a network of several ships operating in the same geographical area, thus experiencing the same sea state. However, the fusion of wave data from multiple vessels positioned far apart from each other in the oceans has so-far been unexplored.

1.2. Content and novelty of study

The proposed concept combines research into the use of ships as wave buoys and the machine learning-driven spatial nowcasting framework established in Chen et al. (2021). In short, this framework relies on a machine learning algorithm which is trained over twenty years of historical wave hindcast data from a physics-based model. The resultant surrogate model learns the spatial relationship between input data at a few (two to three) point locations within a predefined domain to the full spatially distributed wave conditions across the domain. Real-time in-situ observations can then be used as a replacement for the input hindcast data in order to produce immediate, accurate estimates of the wave conditions across a large-extent spatial domain.

While the original study (Chen et al., 2021) was limited to observations from wave buoys, the present paper proposes the inclusion of ship-based measurements as in-situ observations. To evaluate this, a ship-as-a-wave-buoy technique is used to derive theoretical estimates of the wave parameters from the simulated motions of a ship. The reliability of the sea state estimates from the ship is analysed by intercomparison with available buoy data. Subsequently, a surrogate model is developed and operated with the buoy and ship data as in-situ inputs. The model performs the task of nowcasting wave conditions at any point in the domain without running a full spectral wave model. A range of scenarios are presented, analysing the effect of including in-situ data from vessels on the accuracy of the surrogate system. The performance of these surrogate models are benchmarked against the results of the physics-based hindcast model, comparing the output from the models with further buoy measurements at different validation points within the domain.

The remaining part of this paper is organised as follows. After presenting the theoretical background of in-situ SSE techniques (Section 2), the methodology for combining wave buoy and ship-based data is described (Section 3). In Section 4, the results from a hybrid case study – i.e. making use of historical buoy data and numerically simulated records of ship motions – are presented and discussed. Conclusions are included in Section 5.

2. Underlying theory of in-situ sea state estimation techniques

Various techniques exist to analyse the spectral and directional characteristics of a wave field from in-situ sensors, characterising and describing the way the energy (or equivalently the variance) of the wave field spreads over both circular frequencies ω and directions of propagation μ. The underlying theory is well established and reported in several textbooks (e.g. Tucker and Pitt, 2001). As such, the directional wave spectrum $E(\omega,\mu)$, or *2-D wave spectrum*, is considered the fundamental quantity of wave modelling and the quantity that allows the calculation of the consequences of interactions between waves and other phenomena or marine structures (Hauser et al., 2005).

The waves are assumed to be a stationary, ergodic, Gaussian process, as a prerequisite for a description of the wave system in the frequency-direction domain. This ensures that the wave statistics, i.e. the probability density function of the random wave process, are constant. Due to the natural variation of ocean waves, this assumption can only hold over a limited time period, which in practice requires the spectral computations to be performed over consecutive time windows of, say, twenty to thirty minutes (Hauser et al., 2005).

A classical decomposition of the directional wave spectrum is:

$$E(\omega,\mu) = E(\omega)\cdot D(\omega,\mu) \tag{1}$$

where $E(\omega)$ is the (omnidirectional) wave variance spectrum, labelled *1-D wave spectrum* in the present paper. The directional spreading density function (DSF) $D(\omega,\mu)$ may be expressed as a Fourier series, in general dependent on frequency:

$$D(\omega,\mu) = \frac{1}{2\pi} + \frac{1}{\pi}\sum_{n=1}^{\infty}\left\{a_n(\omega)\cos(n\mu) + b_n(\omega)\sin(n\mu)\right\} \tag{2}$$

The DSF satisfies two important properties at any frequency $\omega > 0$:

$$\forall \mu \in [0, 2\pi], \ D(\omega, \mu) \geq 0, \tag{3}$$

$$\text{and} \int_0^{2\pi} D(\omega, \mu) \, \mathrm{d}\mu = 1. \tag{4}$$

From Eq. (4), it follows that the 1-D wave spectrum can be derived from integration of the 2-D spectrum over the directions:

$$E(\omega) = \int_0^{2\pi} E(\omega, \mu) \, \mathrm{d}\mu \tag{5}$$

2.1. Spectral processing of wave buoy measurements

For estimating the full directional spectrum, the maximum entropy principle method (MEP) may be applied when three-quantity (*triplet*) point measurements from a single buoy are available. The MEP was originally developed by Kobune and Hashimoto (1986) but is still considered a powerful means for estimating the full directional spectrum. It is based on the Shannon definition for the entropy function $H(\hat{D})$, given in Eq. (6), which has to be maximised at any frequency under the various constraints given by the buoy measurements for the estimated DSF $\hat{D}$:

$$H(\hat{D}) = -\int_0^{2\pi} \hat{D}(\mu) \ln \hat{D}(\mu) \, \mathrm{d}\mu \tag{6}$$

First, the cross-spectra are computed between each pair of recorded signals using Welch's method of time-averaging over short, modified periodograms (Welch, 1967). The complex-valued cross-spectra for the buoy displacements are denoted $G_{ij}(\omega)$. Since this study uses moored buoys recording the heave, East, and North displacements, the indices i and j are 1 for heave, 2 for East, and 3 for North. The coincident and quadrature spectral density functions $C_{ij}(\omega)$ and $Q_{ij}(\omega)$ are defined as the real and imaginary parts of $G_{ij}(\omega)$, respectively. Assuming an ideal buoy for which the heave displacement follows perfectly the wave surface elevation, the 1-D wave spectrum $E(\omega)$ equals the heave–heave spectrum, which is a real-valued function:

$$E(\omega) = G_{11}(\omega) = C_{11}(\omega) \tag{7}$$

Following Benoit et al. (1997), the first four frequency-dependent Fourier coefficients of the DSF can be computed from the cross-spectral components, as reproduced in Eq. (8):

$$\begin{aligned} a_1 &= -Q_{12}/\sqrt{C_{11} \cdot (C_{22} + C_{33})} \\ b_1 &= -Q_{13}/\sqrt{C_{11} \cdot (C_{22} + C_{33})} \\ a_2 &= (C_{22} - C_{33})/(C_{22} + C_{33}) \\ b_2 &= 2C_{23}/(C_{22} + C_{33}) \end{aligned} \tag{8}$$

Kobune and Hashimoto (1986) demonstrated that a solution to the minimisation problem for the DSF $D(\omega, \mu)$ has the following shape:

$$D = \exp\left(-L_0 - \mathbf{L}^\top \mathbf{q}\right) \tag{9}$$

where $\mathbf{L} = \begin{bmatrix} L_1 & L_2 & L_3 & L_4 \end{bmatrix}^\top$ are unknown functions, called Lagrange multipliers, to be found to satisfy the constraints on the Fourier coefficients given in Eq. (8). The vector $\mathbf{q}$ contains sine and cosine functions of the wave direction μ:

$$\mathbf{q} = \begin{bmatrix} \cos\mu & \sin\mu & \cos 2\mu & \sin 2\mu \end{bmatrix}^\top \tag{10}$$

The Lagrange multipliers can be computed using the Newton method of local linearisation, as described in Hashimoto (1997). Alternatively, Kim et al. (1995) proposed an approximated solution for the Lagrange multipliers:

$$\begin{aligned} L_1 &= 2a_1a_2 + 2b_1b_2 - 2a_1(1 + a_1^2 + b_1^2 + a_2^2 + b_2^2) \\ L_2 &= 2a_1b_2 - 2b_1a_2 - 2b_1(1 + a_1^2 + b_1^2 + a_2^2 + b_2^2) \\ L_3 &= a_1^2 - b_1^2 - 2a_2(1 + a_1^2 + b_1^2 + a_2^2 + b_2^2) \\ L_4 &= 2a_1b_1 - 2b_2(1 + a_1^2 + b_1^2 + a_2^2 + b_2^2) \end{aligned} \tag{11}$$

where it is emphasised that all quantities are frequency-dependent. This approximation scheme removes the convergence problems that may occur with the full MEP implementation in some cases with real sea state data.

L_0 is a normalisation term ensuring that condition of unit integral given in Eq. (4) is verified. It is found to be:

$$L_0 = \ln\left(\int_0^{2\pi} \exp\left(-\mathbf{L}^\top \mathbf{q}\right) \, \mathrm{d}\mu\right) \tag{12}$$

2.2. The wave-buoy analogy for shipboard estimation of wave spectra

Just like a buoy, a ship responds as a result of the incident waves. The WBA aims to use a ship's wave-induced motions for SSE. The standard instrumentation for navigation systems onboard modern ships includes inertial measurement units (IMUs) and global positioning system (GPS) sensors, recording the linear and angular motions (alternatively, accelerations), as well as the course, speed, and geographical position. The surge, sway, and yaw motions can be influenced by the control system (or mooring), if in operation, and these motion components are therefore not necessarily suitable for estimating the incident wave system (Brodtkorb et al., 2018a). The remaining three rigid-body motion components – i.e. heave, roll, and pitch – can be exploited to estimate the sea state, in a similar manner to a moored pitch-roll-heave buoy. One of the main advantages of the WBA lies in that it does not require any additional instrumentation or sensor placement.

In the following, we assume stationary environmental and operational conditions. The heave z, roll ϕ and pitch θ time histories are assumed to be available, sampled at an appropriate frequency f_s, typically around 5–20 Hz. The Welch's method, already introduced in Section 2.1, can be exploited to compute the so-called measured cross-spectra $\tilde{S}_{RR'}$ between two responses $R, R' \in \{z, \phi, \theta\}$, where the tilde indicates that the data is of observational nature.

We further assume that the waves have small steepness, which characterises a low to moderate sea state. This allows modelling the ship as a linear system with respect to the wave excitation (i.e. *input*) and the motion response (i.e. *output*). In this framework, a theoretical estimate $\hat{S}_{RR'}(\omega)$ of the ship cross-spectrum between two arbitrary wave-induced responses R and R' is mathematically obtained in Eq. (13). It is related to the 2-D wave spectrum by use of the complex-valued wave-to-response transfer functions $\Phi_R(\omega, \beta)$ for the concerned responses:

$$\hat{S}_{RR'}(\omega) = \int_0^{2\pi} \Phi_R(\omega, \beta)\overline{\Phi_{R'}(\omega, \beta)} E(\omega, \mu) \, \mathrm{d}\mu \tag{13}$$

where the bar $\overline{(\cdot)}$ indicates the conjugate of a complex quantity and the caret symbol $\hat{(\cdot)}$ implies the estimate is associated with some (model) uncertainty. The relative wave heading $\beta = 180° + \mu - \psi$ is defined as the angular difference between the direction μ where the waves are coming from and the orientation ψ of the ship's bow in a North-East-Down reference frame; as sketched in Fig. 1.

Several difficulties arise when considering a vessel as a buoy; the main challenges being (1) the increased complexity of the ship transfer functions with respect to the hull geometry, compared to those of a buoy having a simple underwater geometrical shape (semi-sphere, etc.); (2) the wave filtering effect, which limits the range of frequencies at which ships have a significant response; and (3) the Doppler shift in the encountered waves in the case of advancing vessels with forward speed. The latter problem was addressed by Iseki and Ohtsu (2000) and Nielsen (2006).

It is interesting to note that the MEP method for spectral analysis of buoy motions cannot be applied directly to the analysis of the triplet motion records from a single ship, because the 1-D wave spectrum $E(\omega)$ is unknown *a priori*, contrary to a buoy for which this quantity can accurately be derived from one of the measured signals (e.g. buoy vertical displacement), since wave filtering is insignificant due to the

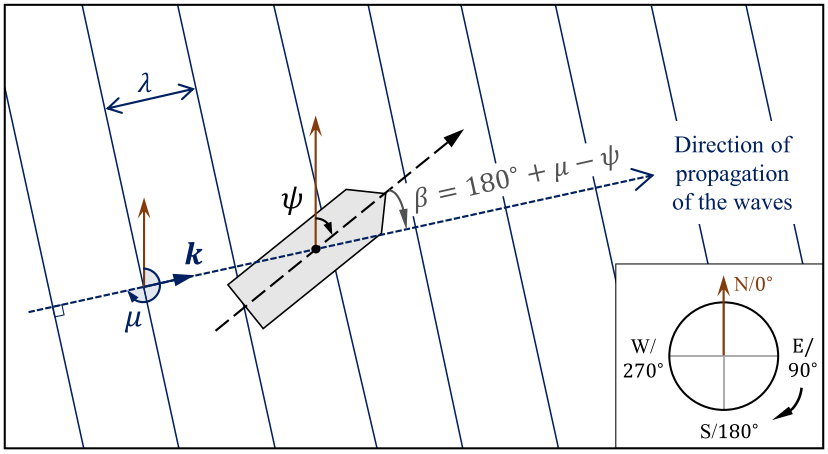

Fig. 1. Definition of the heading angles. The wavelength is denoted λ, and $\mathbf{k}$ is the wavenumber vector. The direction the waves come from is defined by an angle μ relative to North. The ship's bow orientation has an angle ψ with North. The angle of encounter of the waves with the ship's centre-line is labelled β, with clockwise positive orientation, in accordance with the North-East-Down reference frame.

small relative dimensions of a buoy. Nonetheless, there exist many different SSE methods based on measured vessel responses; a comprehensive account is given in Nielsen (2017). The fundamental reasoning behind these mathematical inverse formulations is that the error must be minimised between the measured and theoretical response spectra, i.e. $\tilde{S}_{RR'}$ and $\hat{S}_{RR'}$, respectively, the latter being obtained from Eq. (13) and evaluated with the estimated wave spectrum as input:

$$e_{RR'}(\omega) = \tilde{S}_{RR'}(\omega) - \hat{S}_{RR'}(\omega) \tag{14}$$

This problem involves a number of nonlinear equations to be solved. In the present paper, we employ a *model-based* spectral-residual calculation method formulated in Brodtkorb and Nielsen (2022), which will be summarised in Section 3. Unlike machine learning-based sea state estimation approaches (Mittendorf et al., 2022), the method does not require a large amount of ship response data to be collected prior to actual operation to constitute a training set for a single ship. This is an advantage for the applicability of the proposed framework, because one wants to make *ad hoc* use of ships where/when data is needed.

2.3. Wave system characterisation

In many contexts, including some industrial applications like the planning of offshore operations, full knowledge of the 2-D matrix constituting the directional wave spectrum is not needed. It can instead be more practical to work with a lower number of scalar quantities, namely the integrated sea state parameters, which provide sufficient information to evaluate the associated risk levels of the particular activity to be conducted at sea. Most of these sea state parameters are determined from the spectral moments m_n of the wave spectrum $E(\omega)$, which are defined as the integral $m_n = \int_0^\infty \omega^n E(\omega)\,\mathrm{d}\omega$, and $n \in \{-1, 0, 1, 2\}$ leads to the following parameters, with the mathematical definitions given by Eqs. (15)–(21) (e.g., DNV, 2010): the significant wave height H_s, peak wave period T_p, mean wave period T_{m01}, mean zero up-crossing period T_z, mean energy period T_E, peak wave direction μ_P, and mean overall wave direction μ_m.

$$H_s = 4\sqrt{m_0} \tag{15}$$

$$T_p = 2\pi/(\mathrm{argmax}_\omega\ [E(\omega)]) \tag{16}$$

$$T_{m01} = 2\pi\ (m_0/m_1) \tag{17}$$

$$T_z = 2\pi\sqrt{m_0/m_2} \tag{18}$$

$$T_E = 2\pi\ (m_{-1}/m_0) \tag{19}$$

$$\mu_P = \mathrm{argmax}_\mu\ [E(\omega, \mu)] \tag{20}$$

$$\mu_m = \arctan(d/c) \tag{21}$$

with d and c in Eq. (21) defined respectively as:

$$d = \int_0^{2\pi}\int_0^\infty E(\omega,\mu)\sin(\mu)\ \mathrm{d}\omega\ \mathrm{d}\mu; \quad c = \int_0^{2\pi}\int_0^\infty E(\omega,\mu)\cos(\mu)\ \mathrm{d}\omega\ \mathrm{d}\mu.$$

2.4. Machine learning-based surrogate wave spatial model

The surrogate nowcasting model maps wave data from discrete buoy locations to the sea state conditions of an entire domain; see details in Chen et al. (2021). This surrogate modelling method provides a low-cost hybrid model relying on limited observation data and a physics-based numerical model. It is based on the assumption that a numerical wave model can capture the physics-based spatial correlations within the model domain, in effect employing this high-fidelity numerical modelling as the data generator.

In the design of the surrogate model, machine learning (ML) algorithms are used to learn the relationship between the wave conditions at specific buoy locations and the spatially distributed wave conditions across the entire domain using the outputs of a physics-based numerical model. Once trained, the model predictions generate spatial distributions of the sea state parameters using in-situ measurements as input. The surrogate model diagram is shown in Fig. 2.

As a supervised machine learning model, it is key to select an appropriate input–output formulation. The inputs when training the surrogate model are the physics-based numerical model results extracted at the input buoy locations. As the spatial outputs of the physics-based numerical model contain many output grid points, it is too computationally expensive to work with these directly. Therefore, the surrogate model is trained on a reduced-dimension dataset for computational efficiency. The original high-resolution numerical results were transformed into a reduced-order dataset, satisfying a number of conditions, which include: (1) the approximation error is small; (2) the spatial distribution is preserved as much as possible; and (3) the reduction procedure is computationally efficient. In this work, the bi-linear interpolation method was used to achieve dimension reduction. After prediction, a dimension ascension returns the predictions to the original resolution of the physics-based numerical model. This is described and assessed in greater depth in Chen et al. (2021).

The machine learning algorithm implemented in the surrogate model training is replaceable, meaning that any algorithm that can learn the relationship between input and output can be adopted. In this work, a multivariate Random Forest (RF) (Breiman, 2001) regression method was implemented to train the surrogate model, following the work by Chen et al. (2021). RF is one of the most effective machine learning methods that can achieve nonlinear regression by ensemble multiple parallel decision tree models. The ensemble and random

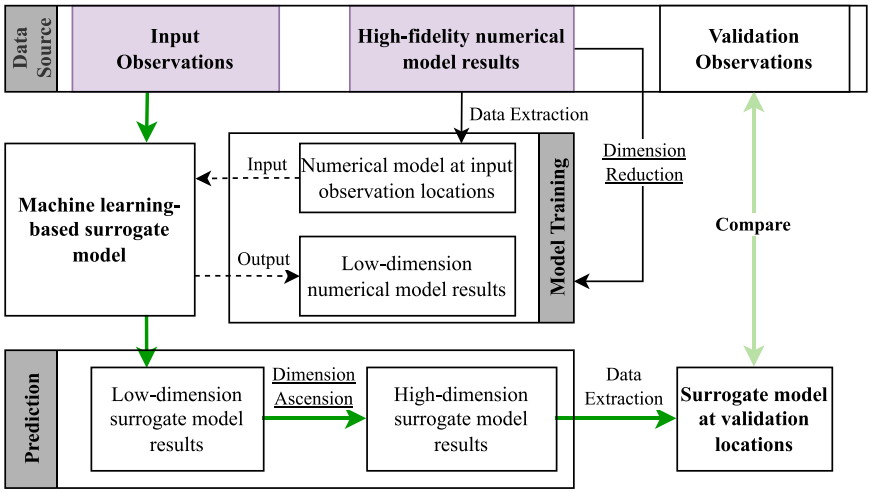

Fig. 2. Overview of the surrogate wave modelling approach. The black arrows represent the processes of surrogate model training, while the green arrows show the processes of the surrogate model prediction. To validate the surrogate model, the outputs are compared against independent buoy measurements.

concepts in RF can greatly reduce overfitting and increase diversity in tree models, and thus make the prediction more robust (Hastie et al., 2009).

2.5. Evaluation criteria

The model outputs were extracted at a set of validation locations and compared with complementary in-situ buoy observations to assess the performance. The assessment of the different models in this study over the validation period utilises four error metrics; the root-mean-squared error (RMSE), mean absolute error (MAE), mean absolute error percentage (MAPE) and coefficient of determination (R^2). RMSE and MAE are scale-dependent, while MAPE and R^2 are dimensionless and scale-independent. The four error metrics (Wilks, 2011) were calculated by Eqs. (22) to (25), respectively.

$$\mathrm{RMSE} = \sqrt{\frac{1}{N}\sum_{i=1}^{N}\left(\mathrm{diff}(\hat{y}_i, y_i)\right)^2} \tag{22}$$

$$\mathrm{MAE} = \frac{1}{N}\sum_{i=1}^{N}\left|\mathrm{diff}(\hat{y}_i, y_i)\right| \tag{23}$$

$$\mathrm{MAPE} = \frac{1}{N}\sum_{i=1}^{N}\left|\frac{\mathrm{diff}(\hat{y}_i, y_i)}{y_i}\right| \times 100 \tag{24}$$

$$R^2 = 1 - \frac{\sum_{i=1}^{N}\left(\mathrm{diff}(\hat{y}_i, y_i)\right)^2}{\sum_{i=1}^{N}\left(\mathrm{diff}(\bar{y}, y_i)\right)^2} \tag{25}$$

where N denotes the number of predicted samples, $\hat{y}$, y and $\bar{y}$ represent the model prediction, the buoy observation, and the mean of buoy observation, respectively. For non-directional data, such as significant wave height and wave periods, the function diff is defined as the direct difference $\mathrm{diff}(x, y) = x - y$. However, for directional data, such as mean wave direction and peak direction, the function is defined as $\mathrm{diff}(x, y) = \arctan(\sin(x - y)/\cos(x - y))$, which computes the minimum angular difference in the range $[-\pi, \pi]$ rad, taking into account how angles wrap around with a modulo of 2π. Moreover, in the computation of R^2, the mean of observed directions is defined as $\bar{y} = \arctan(\sum \sin(y_i)/\sum \cos(y_i))$. Note that the MAPE metric is not used for angular data, because zero (or close-to-zero) angles would yield values of MAPE tending to infinity.

3. Methods and data

This section introduces the proposed methodology and presents a case study that was designed as a proof of concept and validation of the implementation.

3.1. Scope of the case study

The case study is focused on a regional area which was selected to be the same as in the previous work by Chen et al. (2021), namely the water off the southwest coast surrounding Cornwall, UK, as mapped in Fig. 3. This region sits at the easterly extent of the North Atlantic with significant fetch into this active, highly seasonal ocean region. As such, the wave climate is a mix of locally-generated wind waves and incoming swell which is dominated by storms that form in the North Atlantic and propagate through the region. The map in Fig. 3 indicates the location of six wave observation sites, named Penzance, Looe Bay, WaveHub, Perranporth, FabTest, and Porthleven, for all of which historical buoy data is made available by the Channel Coast Observatory[1] (CCO).

In this study, three different topologies of the observation network – corresponding to various surrogate models – are compared, varying the number and nature of the observation platforms. The investigation examines the hypothesis that using the WBA on a vessel within the domain can improve the accuracy of the surrogate model output when a suitable input (buoy) measurement is not available. The overarching aim of this case study is to assess the effectiveness of the WBA when used within the observation network. For that purpose, three different surrogate models are designed: 'Model 1' uses buoy data exclusively, comprising a network of three buoys, and therefore expected to be the best-performing setup; 'Model 2' uses a network of two buoys, in conjunction with observations from one vessel, which replace the actual buoy data collected at one site, for a complete three-point input set; and 'Model 3' uses a network with only two buoys, omitting the site previously used for the observations from the vessel, and expected to be the worst-performing setup. The WaveHub site, located near the north coast of Cornwall, was the chosen location for the vessel-based observations used as a substitute for the buoy data in Model 2, and also the data omitted in Model 3. The two buoys at Penzance and Looe Bay, both located near the south coast of Cornwall, constitute the common part of the input for all three surrogate models. An additional case, 'Model 4', is the physics-based numerical wave model, which will be used as a reference in the comparison of the spatial results from the three surrogate models. This will enable us to finely assess where the performance of Model 2 stands, relative to those of Models 1 and 3. Finally, the remaining three buoys at Perranporth, FabTest, and Porthleven, will be used for local validation of the output results from all four models.

[1] https://coastalmonitoring.org/.

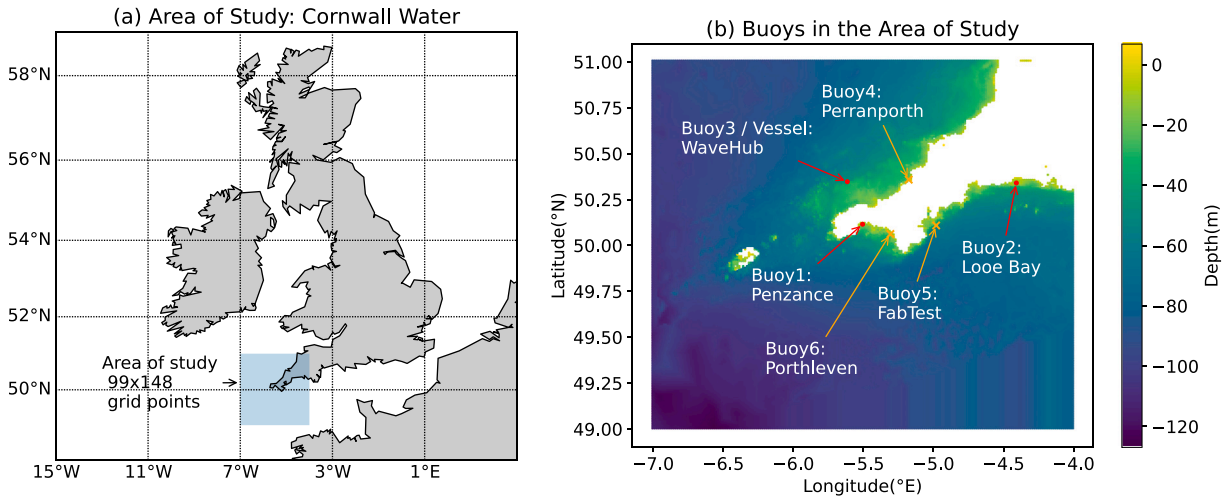

Fig. 3. The area of study is around Cornwall in the UK ranging from 4°W to 7°W in longitude, and 49°N to 51°N in latitude. The three red points (Penzance, Looe Bay, and WaveHub) represent buoys or the proposed 'ship-as-a-buoy' used as inputs for the spatio-temporal model, and the three orange points (Perranporth, FabTest, and Porthleven) represent the buoy locations used for validating the model outputs and benchmarking the proposed model framework.

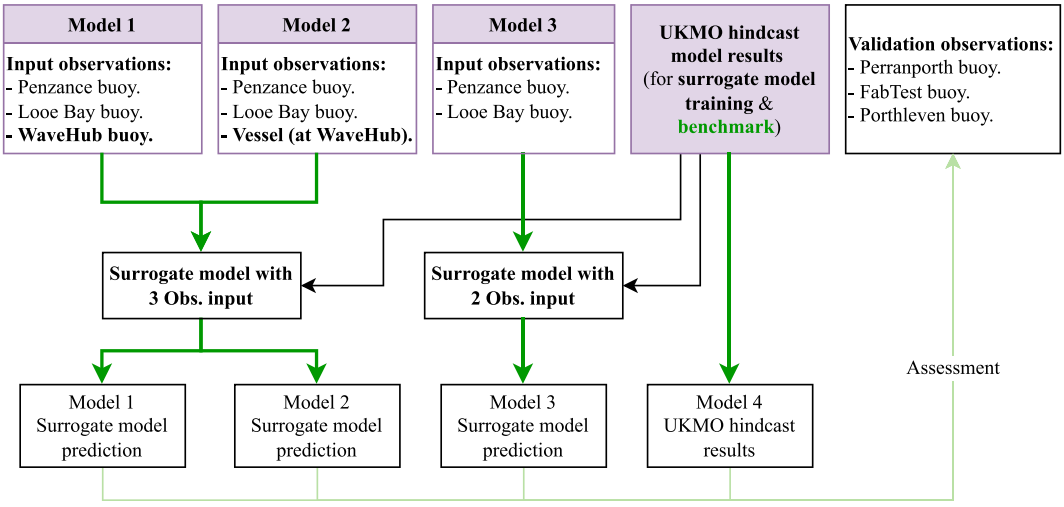

Fig. 4. Scope of the case study flowchart. Black lines refer to the surrogate model training which utilises the UKMO hindcast model results in 1989–2009. Green lines represent the model prediction and validation which focus on the data in 2016. Three surrogate models correspond to three observation scenarios; Model 1: 3 buoys as input; Model 2: 2 buoys + 1 vessel; Model 3: 2 buoys; Model 4: UKMO hindcast. See Fig. 2 for methodological details on the surrogate model training, prediction, and validation steps.

The scope of the case study is illustrated in a flowchart in Fig. 4, and the flowchart serves as a reference for the remainder of this section.

3.1.1. Physics-based numerical wave model

Although the surrogate wave spatial model trained on a SWAN model as presented by Chen et al. (2021) has demonstrated satisfactory results at WaveHub, analysis by Ashton and Johanning (2014) has shown that the SWAN model failed to represent wave systems arriving from the East which can be explained by the underestimation of the wave spectra energy in the low-frequency domain in the SWAN model boundary input. This SWAN model used ERA-Interim boundary input provided by ECMWF (van Nieuwkoop et al., 2013). This misrepresentation of the Eastern boundary can potentially cause in-model errors related to wave period and thus limit the surrogate spatial model's ability to learn the correlations across the domain. Ashton and Johanning (2014) also identified that using a United Kingdom Met Office (UKMO) wave model product at the boundaries could reduce these errors. Therefore, in this study, the UKMO regional wave hindcast product was used to train the surrogate spatial model in place of the SWAN model used in Chen et al. (2021).

The UKMO regional wave hindcast product was generated using a WAVEWATCH III 1.5 km Atlantic Margin Model (Graham et al., 2018) for the Copernicus Marine Environment Monitoring Service,[2] whose spatial domain covers the seas on the North-West European continental shelf from 16°W to 13°E with the resolution of 1.9 ± 0.4 km (1/33°) in longitude and from 46°N to 63°N with the resolution of 1.5 km (1/74°) in latitude. Data are available from 1 January 1980 up until the present with a temporal resolution of 3 h. The model was nested with lateral boundary conditions supplied from a Met Office global wave model hindcast, driven by the ECMWF ERA5 wind fields.

The UKMO wave hindcast model provides integrated wave parameters computed from the directional wave spectrum. This work considers H_s, T_p, T_z, T_E, and μ_m, all mathematically defined in Section 2.3. The accuracy of UKMO model results against observations varies from open waters to regional areas. The correlation coefficient of H_s ranges from 0.95 or better to 0.90–0.95, T_z ranges from 0.86–0.95 to 0.71–0.89, T_p ranges from 0.71–0.86 to 0.66–0.82. And due to the lack of directional wave data from open waters, the model biases of μ_m are within +/−

[2] http://marine.copernicus.eu/.

Table 1
Location of the buoys used in this study.

No.	Buoy	Lat [°N]	Lon [°W]	Depth [m] (Approx.)	Distance from the nearest UKMO numerical model grid point [km]
1	Penzance	50.1	5.5	10	1.09
2	Looe Bay	50.3	4.4	10	0.95
3	WaveHub	50.3	5.6	50	0.76
4	Perranporth	50.4	5.2	14	5.50
5	FabTest	50.1	5.0	30	0.85
6	Porthleven	50.1	5.3	15	1.95

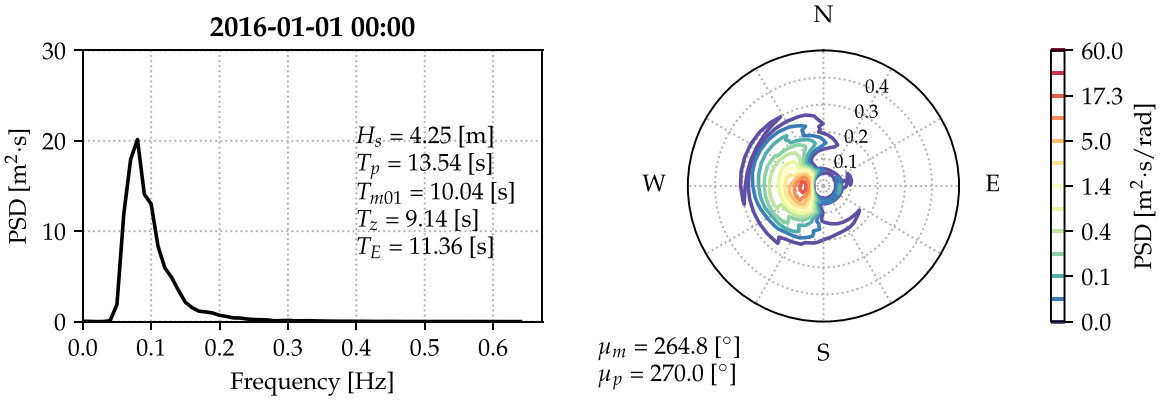

Fig. 5. 1-D (left) and 2-D (right) post-processed wave spectra from the buoy measurements on January 1st, 2016 (midnight), at WaveHub. For the 2-D spectrum: radial divisions every 0.1 Hz, circular divisions every 30 degrees, and direction of waves 'coming from' in the North-East-Down reference frame.

10 degrees with a standard deviation equivalent to around 33%–55% of the observation standard deviation (Saulter, 2021).

3.1.2. In-situ observations

Wave data used in this study were recorded in the year 2016 at different buoy locations using Datawell Directional WaveRider MkIII buoys[3]; see locations on the map in Fig. 3 and Table 1.

The buoy at WaveHub was owned by Wave Hub Ltd and operated by CCO, who provided historical data for the year 2016. The dataset includes time series of the heave, East, and North displacements, obtained after filtering and double-integrating the accelerations measured by accelerometers onboard the Datawell buoy at a sampling rate of 3.84 Hz over segments of 30 min. The data is subsequently filtered and downsampled to 1.28 Hz, resulting in 2304 samples per segment (Datawell, 2020). The segments are timestamped at the start of the measurement burst. To construct the buoy cross-spectra, Fourier analysis is performed on 18 consecutive blocks of 100 s worth of wave displacements (i.e. 128 samples for each block), on which a Hanning window is applied for tapering. The resulting 18 spectra are then averaged to compute the post-processed half-hourly spectra. The MEP procedure detailed in Section 2.1 is followed to compute the directional spreading function, with the approximated scheme for the Lagrange multipliers, as presented in Eq. (11), used. The resultant directional wave spectrum comes in a discretised form with 128 frequency bins ranging from 0 to 0.64 Hz, and 36 direction bins from 0 to 350 degrees. In order to remove some of the noise that alters the directional spectra, the spectro-angular matrix $E(\omega_i, \mu_j)$ is filtered by 2D discrete convolution with a 3×3 cell rectangular smoothing window that averages all immediate neighbours of a central bin, as described in Portilla et al. (2009). This operation is realised in Python 3 with the `convolve` function, which is part of the multidimensional image processing library of SciPy (Virtanen et al., 2020). Fig. 5 shows an example plot of the 1-D and 2-D wave spectra, with associated sea state parameters calculated from Eqs. (15) to (21).

[3] https://datawell.nl/products/directional-waverider-mkiii/.

Fig. 6. NTNU's research vessel, Gunnerus.

3.1.3. Ship of study

In the present paper, time-domain simulations are performed for a multipurpose research vessel, Gunnerus (labelled 'RV' onwards), which is owned by the Norwegian University of Science and Technology (NTNU). A photograph of this vessel is shown in Fig. 6 and its main dimensions are given in Table 2. For the specific case study, the RV is assumed to be conducting DP (dynamic positioning) operations and the forward speed is thus taken to be zero. The first-order heave, roll, and pitch motions of the ship are simulated in short-crested wave conditions as given by the (post-processed) 2-D wave spectra at the WaveHub location. The linear wave-to-motion transfer functions have been computed using a strip theory code (ShipX; Fathi, 2018). The amplitude information of the transfer functions is plotted for various relative wave headings in Fig. 7. Note that the ship is port-starboard symmetrical.

The ship heading is constant, set to $\psi = 0$, meaning that the bow is pointing North. A large number of wave components – namely 500 components for each of the 36 discretised directions – is extracted from

Table 2
Principal particulars of the considered vessel for simulations.

	RV
Length overall, L_{oa} [m]	31.25
Length between perpendiculars, L_{pp} [m]	28.90
Breadth middle, B [m]	9.60
Draught moulded, T [m]	2.63
Displacement, Δ [t]	418.06
Block coefficient, C_B [–]	0.559

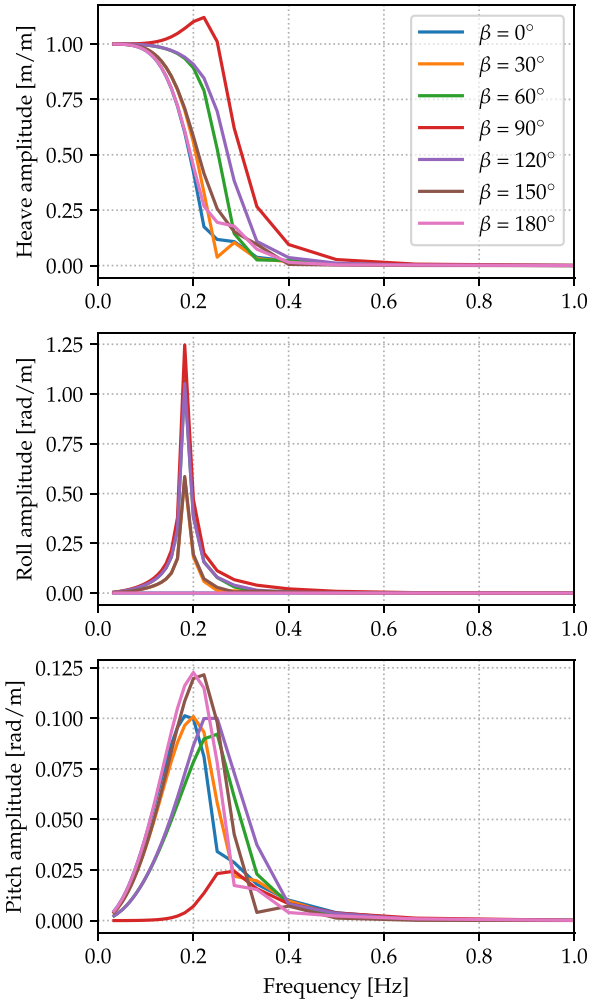

Fig. 7. Amplitude of the wave-to-motion transfer functions for the heave, roll, and pitch motions of RV at various relative wave headings β and zero forward speed $U = 0$.

the buoy 2-D wave spectra, via linear interpolation of the power spectral density (PSD). The component frequencies are randomly picked in the range $[0, 0.64]$ Hz to avoid any repetition in the simulated time series. The phase of the individual components are uniformly distributed in the range $[0, 2\pi]$ rad. Different random seeds are utilised to generate a total of ten 30-min time series of the vessel motions, noticing that the use of different random seeds partly ensures statistically representative results. The Python package that was developed for the ship motion simulations is publicly available.[4]

[4] https://gitlab.gbar.dtu.dk/regmo/NetSSE.git.

3.2. Sea state estimation method from ship motions

As indicated in Section 2.2, the method developed by Brodtkorb and Nielsen (2022) is employed to derive sea state estimates from the simulated ship motions. It assumes that the waves are long-crested, meaning that the response spectra are treated as though they were the result of wave excitation coming from one single direction. This assumption represents a limitation in itself because the method is only able to return a point-wise (or 1-D) estimate of the wave spectrum, together with an estimate of the wave direction. In other words, no information on directional spreading can be derived. However, it is emphasised that the proposed networked estimation framework focuses on nowcasting the sea state parameters for the total wave system as defined in Eqs. (15) to (20), excluding the mean directional spreading and disregarding any partitioning between wind sea and swell systems. The chosen SSE algorithm is therefore well suited for the particular application.

An illustration of the SSE algorithm is given in Fig. 8. The input consists of the ship transfer functions $\Phi_R(\omega, \beta)$ and the recorded response time series for the heave z, roll ϕ, and pitch θ motion components. First, the motion cross-spectra $\tilde{S}_{RR'}(\omega)$ are computed. Then, an iterative procedure is run to produce candidates of the wave spectrum for each possible (relative) wave heading β. In each iteration, the error $e_{RR'}(\omega)$ between the response spectra – as defined in Eq. (14) – is evaluated and a portion of it (determined by the gains $h_{RR'}$) is re-injected into the wave spectrum estimate for updating. When the error becomes lower than a given tolerance threshold $\epsilon_{RR'}$, or if the set maximum number of iterations is exceeded, the loop stops and returns the spectrum candidates $\hat{E}_{RR'}(\omega; \beta)$. A wave direction candidate is selected as the one direction in the range $[0, 90°]$ that minimises the energy discrepancy between spectrum estimates over the set of considered responses $RR' \in \{zz, z\phi, z\theta, \phi\phi, \phi\theta, \theta\theta\}$. Port/starboard and following/head waves are distinguished by analysis of the sign of the imaginary part of the heave-roll and heave-pitch cross-spectra, respectively. The wave spectra corresponding to the estimated relative wave heading $\hat{\beta}$ are fused together for the six different response pairs RR' by averaging with equal weight, which finally forms the 1-D wave spectrum estimate $\hat{E}(\omega)$. The integral sea state parameters are derived from the latter as described in Section 2.3. The reader is referred to the original studies for further details on the implementation of the algorithm. In the present study, the maximum number of iterations was set to 200. The gains are automatically adjusted to 50% of the maximum value ensuring stability, as explained in Brodtkorb and Nielsen (2022), and the tolerances are specified as 10% of the peak amplitude in the response cross-spectra.

The sea state estimation methodology is generic and applicable to any ship as long as accurate wave-to-motion transfer functions are available for the given ship and operational conditions. In this study, the uncertainty of the vessel model is circumvented by using the *very same* set of transfer functions for the simulations of vessel motions, on the one hand, and for the sea state estimation algorithm, on the other hand.

3.3. Implementation of the surrogate model

Following the work by Chen et al. (2021), the multivariate Random Forest regression algorithm with the same hyper-parameter was used to train the surrogate model for the present paper. To be consistent with the surrogate model trained by SWAN model results (Chen et al., 2021), the UKMO hindcast data were trimmed to the same target region as the SWAN model but with UKMO model spatial resolution (Fig. 3), resulting in 99 × 148 cells in the grid, and the years from 1989 to 2009 were selected as the training dataset. To keep a similar dimension of surrogate model output as in the previous work, 1/3 scaling was selected. The dimension change (reduction and ascension) through bi-linear interpolation can be seen in Fig. 9.

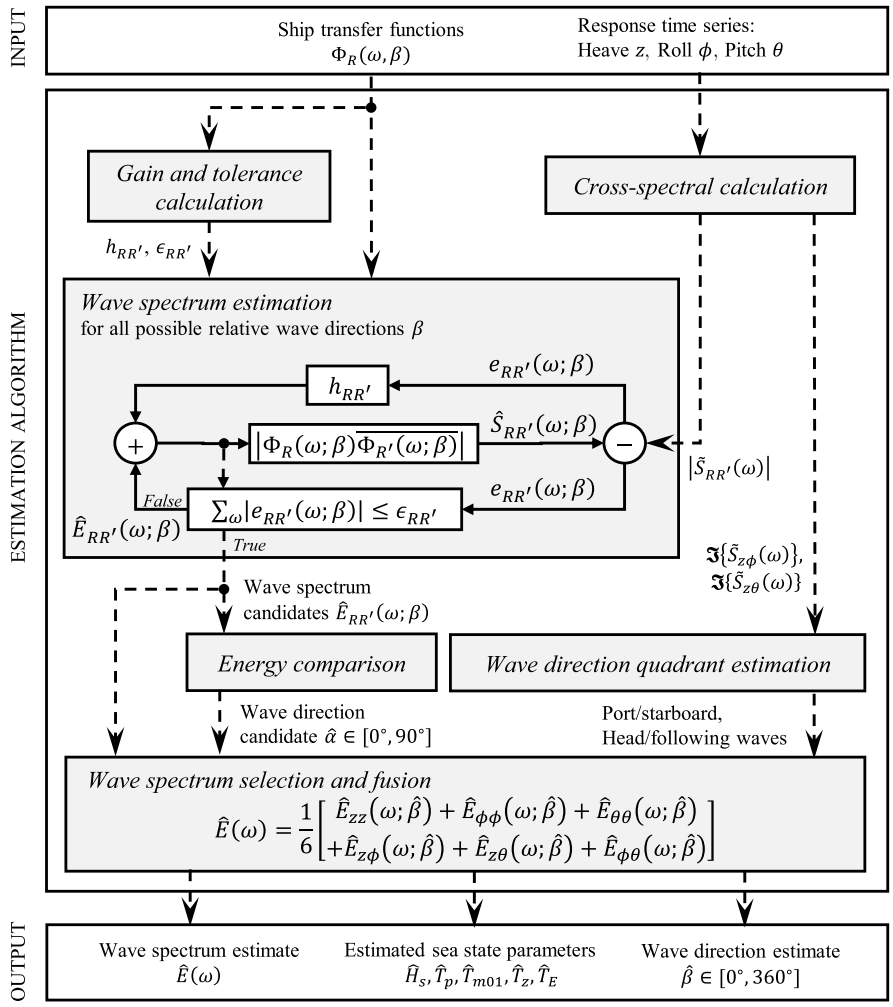

Fig. 8. Illustration of the sea state estimation algorithm proposed in Brodtkorb and Nielsen (2022). There are three main steps: firstly, cross-spectra and algorithm gains and tolerances are calculated; then, the wave spectrum candidates are calculated in the main estimation step; finally, the energy-averaged wave spectrum, direction, and sea state parameters are calculated. The symbol $\Im\{...\}$ denotes the imaginary part of a complex quantity.

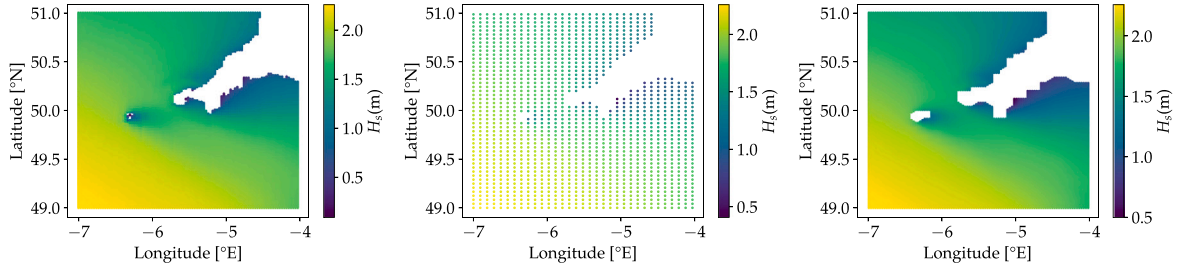

Fig. 9. Resolution comparison between Original grid (left; with a resolution of `latitude segments` × `longitude segments` = 148 × 99), Dimension Reduction (centre; 49 × 33) and Dimension Ascension (right; 148 × 99) for surrogate model. The ML-based model was trained on the reduced resolution data, and the spatial results at low resolution were ascended to high resolution for comparison. The plot here is an example of the comparison representing H_s at a specific time.

The details of the three surrogate models are shown in Table 3. In Model 2, the wave parameters at WaveHub location are observed by the ship, following the methodology described in Section 3.2. The UKMO hindcast model (Model 4) was included in the comparison as a benchmark.

When generating the input and output of the surrogate model, five wave parameters consisting of H_s, T_p, T_z, T_E, and μ_p were considered. Each output wave parameter was modelled in a separate model, i.e. each spatially distributed parameter was predicted simultaneously at all grid points, while all five wave parameters were always considered as inputs. In the surrogate models, wave parameters from the buoys were obtained by spectral processing of the buoy measurements as described in Section 2.1, and the wave parameters from the vessel were estimated by the WBA as introduced in Section 2.2.

4. Results and discussion

4.1. Uncertainty of the spectral estimates from the ship

Ocean waves have properties of a random process, therefore a certain sampling variability of the estimated spectra and sea state parameters is unavoidable (Krogstad et al., 1999). It is essential to

Table 3
Experiment model list. Models 1 to 3 are surrogate models using different buoys as inputs. Both the input and output include the same five wave parameters, i.e. H_s, T_p, T_z, T_E, and μ_p. Model 4 represents the UKMO hindcast model which works as a benchmark of the surrogate models.

	Model 1 (3 buoys input)	Model 2 (2 buoys + 1 vessel input)	Model 3 (2 buoys input)	Model 4
Model description	Surrogate spatial wave model trained on UKMO hindcast results (1989–2009)			UKMO hindcast model
Model training input	Hindcast wave parameters at 3 buoy locations: Penzance, Looe Bay, WaveHub		Hindcast wave parameters at 2 buoy locations: Penzance, Looe Bay	
Model training output	Hindcast spatial wave data, i.e. wave parameters at all grid points within the study area			
Model validation input (observations in 2016)	Penzance (buoy), Looe Bay (buoy), WaveHub (buoy)	Penzance (buoy), Looe Bay (buoy), WaveHub (*vessel*)	Penzance (buoy), Looe Bay (buoy)	
Model output	- Spatial wave data in 2016; - Validation at buoy observations from Perranporth, FabTest, and Porthleven			

quantify this variability for assessing whether observed differences between the ship and buoy estimates at the WaveHub location are statistically significant or not.

The simulation results enable comparisons between three spectral quantities: (1) the target (or, *observed*) 1-D buoy spectrum $E_{\text{buoy}}(\omega)$; (2) the *simulated* wave spectrum $\hat{E}_{\text{simul}}(\omega)$ computed from one time-domain realisation of the surface elevation for the target spectrum; (3) and the *ship-estimated* spectrum $\hat{E}_{\text{RV}}(\omega)$ produced from the SSE algorithm in which the (simulated) ship motion cross-spectra are used as input. It is demonstrated in Chapter 8 of Bendat and Piersol (2011) that, for a given frequency ω, the auto-spectral density estimate obtained by the Welch's averaging method of modified periodograms is a (scaled) chi-square variable with ν_e degrees of freedom. The parameter ν_e corresponds to the equivalent number of independent periodograms (or, segments) used in the averaging process to obtain a smooth spectrum. If (for example) a Hanning window is applied to 50%-overlapping segments, then the segments are partially correlated and ν_e reaches $\nu_e \approx 1.89\nu_d$, where ν_d is the number of disjoint (i.e. non-overlapping) segments of the same size that would fit in the record's duration (Chapter 10 in Brandt, 2011).

We define the random variable ξ_ω as the logarithmic ratio $\xi_\omega = \ln\left(\hat{E}(\omega)/E_{\text{buoy}}(\omega)\right)$ of the estimated spectral ordinates over the buoy-observed ones for a fixed frequency ω. The use of the logarithm in ξ_ω makes the probability density more symmetric about its mean, which, according to Krogstad et al. (1999), facilitates a first-order approximation of ξ_ω as a Gaussian variable with mean $\mathbb{E}[\xi_\omega] = (-1/\hat{\nu}_e) + (1/\nu_{e,\text{buoy}})$ and variance $\text{Var}[\xi_\omega] = (2/\hat{\nu}_e) + (2/\nu_{e,\text{buoy}})$, where $\hat{\nu}_e$ is the number of degrees of freedom for the estimated spectral ordinates, and similarly, $\nu_{e,\text{buoy}}$ is the counterpart for the buoy-observed spectra. This approach therefore also accounts for the statistical uncertainty in the buoy spectra. In this study, the buoy spectra estimates were obtained using a Hanning window over 18 non-overlapping segments, i.e. $\nu_{e,\text{buoy}} = \nu_{d,\text{buoy}} = 18$, while the simulated spectra used 15 segments with a 50% overlap and a Hanning window too, i.e. $\hat{\nu}_e = 1.89 \cdot (15 + 1)/2 = 15.12$.

Fig. 10 shows the statistics of the log-ratios for the simulated ('simul.') spectra and for the ship-estimated ('RV') ones, both of them relative to the buoy spectra. It is important to note that, at low frequencies, the log-ratio is not a meaningful measure since there is low energy in the buoy spectra, i.e., we divide by a small number. Therefore, only the frequencies that lie on the right-hand side of the spectral peak frequency in a given buoy spectrum are accounted for in the frequency-wise statistical analysis of the log-ratio. In the studied buoy data, it appears that all peak frequencies are greater than 0.05 Hz, hence no data is considered at frequencies under this threshold.

The lighter area in Fig. 10 represents the theoretical 95%-confidence interval inside of which one would expect 95% of the samples to have their value of ξ_ω, assuming the above-mentioned Gaussian distribution. It can be seen that the percentiles and mean of ξ_ω for the simulated spectra (in blue) match the theoretical values throughout the frequency

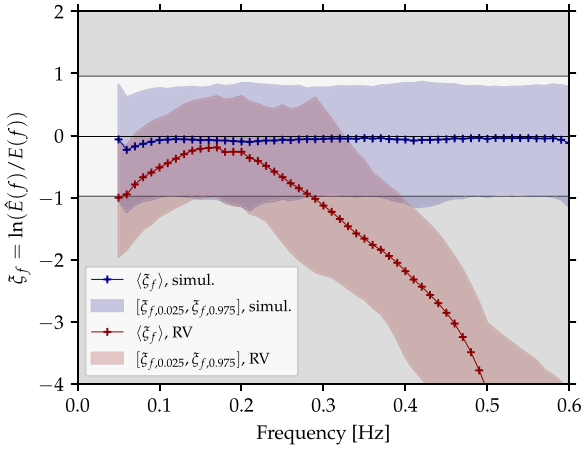

Fig. 10. Statistics of the log-ratio ξ_f of the ship-estimated spectral ordinates over the buoy-observed ones, as a function of wave frequency, for the month of December 2016 at the WaveHub location, Cornwall, UK. The theoretical confidence interval and systematic bias due to sampling uncertainty is displayed with the light area and black solid lines, assuming a Gaussian distribution of the log-ratio. The 2.5-percentile, mean, and 97.5-percentile of the log-ratio are shown for both the purely simulated wave spectra ('simul.', blue curves) and for the ship-estimated ones ('RV', red curves) in the numerator of ξ_f. In both cases, the buoy-observed spectral ordinates are used in the denominator. All ten seeds are included in the dataset, but only at those frequencies that lie on the right-hand side of the spectral peak frequency.

range 0.05–0.60 Hz reasonably well. The discrepancies, and especially the slight asymmetry of the actual distribution about the mean, could be explained by the first-order approximation of ξ_ω as a Gaussian-distributed variable. Moreover, the small fluctuations are due to the inherent randomness and would be expected to disappear asymptotically with an infinite number of samples. It can be concluded that the simulated wave spectra are statistically equivalent to the target buoy spectra, in the sense that there is no significant bias introduced at this point and the variance levels can be entirely explained by the sampling variability predicted from theory.

Considering the ship estimates (cf. red-coloured items in Fig. 10), a negative bias appears throughout the frequency range, but more significantly at the wave frequencies under 0.1 Hz and above 0.2 Hz. This means that at such frequencies, the ship-estimated wave spectra tend to have lower PSD levels than the buoy spectra. Since the SSE algorithm was run using the same vessel transfer functions as for simulating the motions, the model uncertainty can be attributed entirely to the wave filtering effect of the ship – modelled as a linear system – at the designated frequencies; this will be further discussed in Section 4.2. The frequency bandwidth is also confirmed from Fig. 11, where it is seen that the proportion of spectral ordinates having ξ_ω values within the 95%-confidence interval only reaches approximately 95% in the frequency range 0.12–0.20 Hz. The proportion decreases significantly

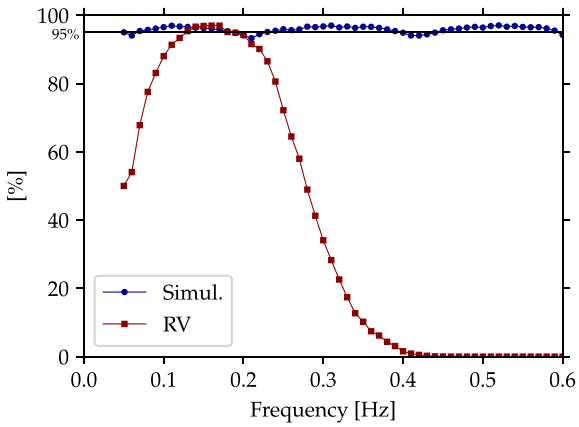

Fig. 11. Proportion (in percent) of the spectral ordinate samples that lie within the theoretical 95% confidence interval of the log-ratio ξ_f as a function of wave frequency, over the month of December 2016 at the WaveHub location, Cornwall, UK. This percentage is computed for the log-ratios involving the purely simulated wave spectra ('Simul.'), as well as for those concerning the ship-estimated spectra ('RV'). All ten seeds are included in the dataset, but only at those frequencies that lie on the right-hand side of the spectral peak frequency.

when it is evaluated away from this frequency range. In comparison, the proportion for the simulated wave spectra remains mostly stable at a level of 95% within the range 0.05–0.60 Hz. Although all the above comments stem from an analysis of the December 2016 data, the data for the other months (not shown) had similar trends.

4.2. Uncertainty of the sea state parameters from the ship

The sea state parameters estimated from the research vessel at the WaveHub location are now assessed by comparison with the buoy observations, referred to by 'MEP', at the same location. Fig. 12 shows the time histories of the integral parameters defined in Section 2.3. A large variety of sea states – in terms of wave heights and periods – are experienced during the observation period (2016), although the (mean) wave direction is mostly centred around $\mu = 270°$ (meteorological convention – direction waves coming from). The latter corresponds to beam sea conditions for the ship, with waves coming from the port side, i.e. with a relative wave heading $\beta = 90°$. At such a heading, the amplitude of the ship transfer functions, Fig. 7, shows that energy is passed from the waves to the ship motions at frequencies up to 0.5 Hz, with substantial response amplification in heave and roll around 0.2 Hz, but overall low response levels in pitch.

The simulations can, again, be used to compute the expected sampling variability in the estimates. The wave parameters were derived using Eqs. (15) to (19) for the simulated wave spectra $\hat{E}_{\text{simul}}(\omega)$, for all seeds. For a given sea state, the sampling variabilities of a wave parameter X derived from two different seeds i and j are assumed to be equal but independent, with a same expectation $\mathbb{E}[X_i] = \mathbb{E}[X_j] = \mathbb{E}[X]$, and a standard deviation that increases linearly with the expectation, i.e. $\text{std}(X_i) = \text{std}(X_j) = \text{COV}(X) \cdot \mathbb{E}[X]$. The coefficient of variation $\text{COV}(X)$ was estimated for each sea state as the sample standard deviation divided by the sample mean over ten seeds. The COV had values of 5%–6% for the significant wave height, 8%–9% for the peak wave period, and 3%–4% for the other period parameters. Considering the buoy parameters X_{buoy} as a reference, it is expected that approximately 95% of the simulated sea state parameters lie within the confidence region delimited by the two straight lines defined as:

$$y_{\pm} = \tan(\pi/4 \pm \delta)\ x_{\text{buoy}},$$
$$\sin(\delta) = \gamma_{0.95} \cdot \text{COV}/2^{1/2},$$
$$\Phi(\gamma_{0.95}) = (0.95 + 1)/2,$$

where Φ is the cumulative standard normal distribution function (Krogstad et al., 1999).

Fig. 13 shows the correlation between the ship estimates and the buoy observations. The confidence region is delimited by the two thin black lines for each parameter — except for the wave direction μ, for which the sampling variability model does not apply. It is seen that the significant wave height and all four period parameters have additional variability that cannot be accounted for by the sampling variability. The mean energy period appears to be the one parameter with the least bias and least scatter. The mean wave period and zero up-crossing period have a positive bias that increases towards lower periods (corresponding to higher wave frequencies). This can be explained by the fact that T_{m01} and T_z rely on the m_1 and m_2 spectral moments, which, compared to m_{-1} and m_0 for T_E, give more weight to the PSD at higher frequencies, where inaccuracies are observed in the ship spectral estimates due to wave filtering, as discussed in the previous section.

It is clear that the significant wave height estimate is biased, also as a consequence of wave filtering, with a negative proportional bias of around 21.6% of the H_s-value calculated by linear regression. This is a major inconvenience in connection with the provision of wave forecasts for the offshore and maritime industries because it could lead to an under-evaluation of the risks. On the other hand, this systematic bias could be corrected by re-calibrating the H_s-estimate from the ship, with any more elaborate consideration therefore an area for future work. Wave filtering is a well-studied phenomenon (Anderson et al., 2016), albeit able to be overcome by adding additional sensors (Nielsen, 2007; de Souza et al., 2017). Previous work on weight-averaging the spectral estimates derived from multiple ships sailing in the same immediate area has shown great potential in attenuating the impact of filtering on the combined output (Nielsen et al., 2019; Mounet et al., 2022).

The randomness introduced in the time-domain simulations can result in a predominant wave system that irregularly switches between coexisting wind sea and swell systems, depending on the seed, which can cause a mismatch in the μ and T_p values between the simulated data and the target sea state. Although a large proportion of the peak period estimates from the ship lies within the confidence region due to this sampling variability, it is observed that many data points significantly underpredict the peak period. The mean absolute proportional deviation (MAPE) between the T_p values of the simulated waves and the target sea state was found to be 11.44%, compared to the 12.61% for the MAPE of the ship estimates. This increase in the error cannot be explained by the spectral moments, because T_p only depends on the location of the peak in the frequency range, independently of the spectral shape. Instead, this could be related to the chosen SSE method, especially because it assumes long-crested waves. It is clear from the ship transfer functions that some wave directions result in larger response amplitudes than others. Therefore, the wave direction[5] and peak wave frequency estimates from the chosen ship-as-a-wave-buoy technique will not necessarily match the predominant wave direction and frequency in the target sea state, and could instead match another wave system (with different peak direction and frequency) that induces responses with similar amplitude levels. In other terms, some scenarios may lead to ambiguous estimates due to the assumption of long-crested waves, which makes it impossible for the SSE algorithm to identify and separate the joint effects that the multiple peaks of a multi-modal wave spectrum have on the induced spectral responses. This supposition could be verified by comparison with results from other ship-as-a-wave buoy techniques that do not assume long-crested waves (Iseki and Ohtsu, 2000; Tannuri et al., 2003; Nielsen, 2006). All related considerations are out of the scope of the present paper and are left for future work.

[5] Due to the assumption of long-crested waves in the SSE algorithm, the wave direction estimated from the ship can be considered as either a mean direction or a peak direction. This choice for the intercomparison with buoy measurements was seen to have very little importance on the results.

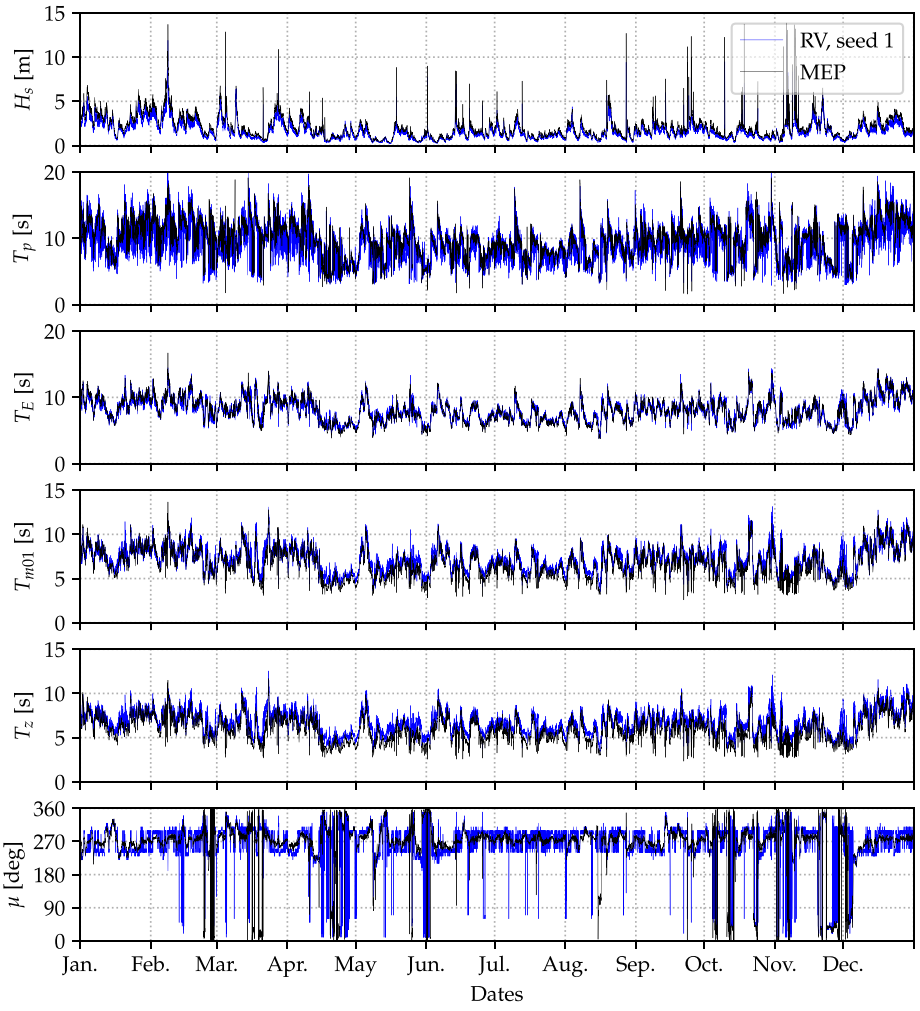

Fig. 12. Ship (blue) and buoy (black) observation data during the year 2016 at the wave buoy location close to WaveHub, Cornwall, UK. The ship-estimated parameters are represented for one seed.

4.3. Spatial results from the network-based sea state estimates compared with UKMO hindcast

The fidelity of the surrogate model is now evaluated with respect to the physics-based model. A point-wise comparison of the spatial output results between the different surrogate models and the UKMO hindcast data is presented here. At each grid point in the computational domain, the annual-averaged RMSE of the H_s and T_E parameters between the surrogate models (i.e. Models 1 to 3, defined in Table 3) and the UKMO model (Model 4) is calculated, and the resulting distributions are visualised by heatmaps in Fig. 14. Note that, for Model 2, the vessel-based input uses data from only one seed.

First, the performances of Models 1 and 2 are compared to evaluate how accurate the WBA system is when integrated into the surrogate model, i.e. how well the input from the vessel in Model 2 replicates the wave buoy of Model 1. The comparison of the spatial distributions of the H_s-error from Figs. 14(a) and 14(c) indicates that Model 1, with inputs from three buoys deployed on both the north and south coasts, features a smaller overall deviation with the UKMO hindcast model, compared to Model 2. Model 1 also shows a more uniform spatial distribution, with the RMSE of H_s remaining at evenly low levels across the domain. In comparison, Model 2, which does not have buoy input on the northern coast, but instead uses the WBA at WaveHub, is characterised by substantial variations of the error for H_s. The accuracy varies notably between the northern and southern coastal areas. It can be said that the H_s-estimates from Model 2 present a significant error across the northern part of the domain, especially nearer to the vessel input where the RMSE reaches almost 0.6 m. This is due to the wave filtering effect inherent to the application of the WBA, which, as mentioned, tends to underestimate the variance of the wave spectrum estimated from ship responses. On the other hand, regarding the estimation of T_E, Model 2 performs almost as well as Model 1, with very similar patterns and levels of the T_E-error for the two models. Referring back to the WBA results from the previous Section 4.2, the parameter T_E, which is less influenced by the wave filtering effect than the other wave parameters, was identified as the most reliable parameter derived from the ship. The spatial result displayed in Fig. 14(d) is promising because it shows evidence that input from a ship can be used in substitution of a "sophisticated" wave buoy in the observation network to estimate – among other parameters – the wave energy period across an extended spatial domain with an analogous level of accuracy.

Next, a comparison of the results from Models 2 and 3 is made to see how much benefit having a vessel in the right place offers to the surrogate system, noting here that Model 3 receives no input at all from the north coast. Overall, it can be said that the spatial results from Model 2 are better than those from Model 3. Regarding the estimation of H_s, it is interesting to notice on Figs. 14(c) and 14(e) that both Models 2 and 3 seem to perform better near the south coast, compared to the north coast. Similar observations can be made on the lee-side of the Isles of Scilly, the westerly archipelago off the Cornish coast, where the RMSE for H_s approaches zero. Generally, it seems that the two models that do not involve buoy observations at WaveHub produce

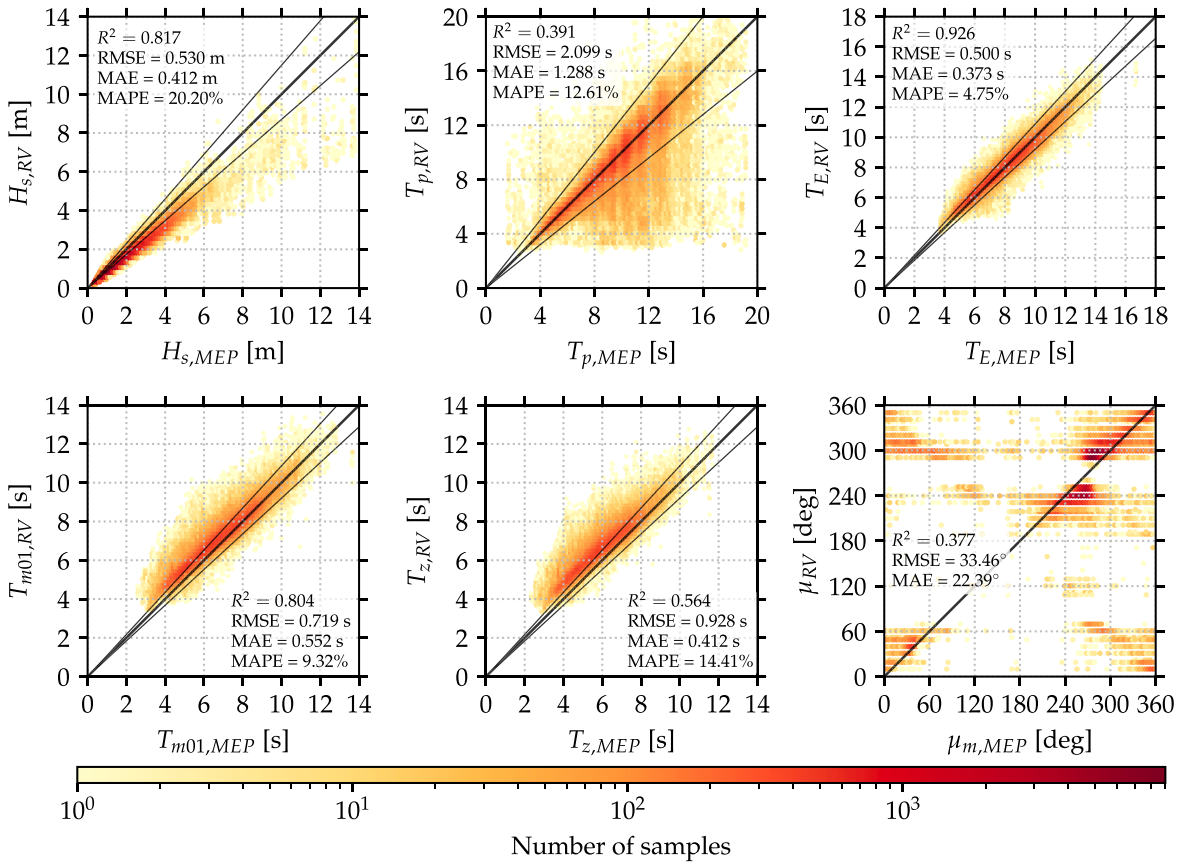

Fig. 13. Two-dimensional hexagonal binning plots between the buoy-estimated (x-axes) and the ship-estimated (y-axes) sea state parameters. The represented data includes ten seeds of the ship estimates at the WaveHub location during the year 2016. The colour intensity is mapped with the density of 30-min samples (in logarithmic scale) within hexagonal cells in the (x, y) plane. The thin black lines indicate approximate 95% confidence limits due to sampling variability only (not applicable for μ).

more reliable H_s-estimates in the more sheltered areas of the domain, which could be explained by a weaker spatial correlation between the wave conditions in these areas and those at the WaveHub location. The latter hypothesis is also supported by Fig. 14(f), where it can be noticed for Model 3 that the sheltered areas have lower RMSE values for the T_E variable than in the remaining of the domain, where the model clearly has poorer performance than Model 2. Therefore, it is fair to say that vessel-based sea state estimates collected at well-chosen positions can advantageously complete a network of buoys to increase the accuracy of spatial estimates in locations where buoy data is scarce.

Ultimately, it is inferred that, although buoy data remains a preferred method for wave estimation, vessel-based data incorporated into the observation network can either serve as an adequate substitute for buoy data when the latter is unavailable, or as an additional source of wave information at a suitable location, for instance where the buoy coverage is sparse.

4.4. Validation results against buoy observations

The model output results of all five wave parameters are now analysed by intercomparison with actual buoy observations at three validation points, namely Perranporth, Porthleven, and FabTest. The closest grid points to the buoy locations were used for the comparison. The error metrics defined in Section 2.4 are computed for the four models and gathered in Table 4. In order to better visualise the comparative performance trends of the four models, quantile–quantile (Q-Q) plots are given in Fig. 15 to show the correlation between the individual model outputs and the buoy observations at Perranporth. Additional validation results are provided for Porthleven and FabTest locations in Appendix.

Generally, for all five wave parameters, Model 1 has lower error values than Model 2 at Perranporth and Porthleven validation points. In fact, Model 1 achieves similar levels of accuracy and precision to the UKMO hindcast model at those two locations. The differences between Models 1 and 2 are most significant for H_s, T_z, and T_p parameters at Perranporth, and for H_s at Porthleven, with increases in the MAPE values of factors of 1.4–1.8 from Model 1 to Model 2. The Q-Q plots (cf. Fig. 15) at Perranporth – which is the closest validation point to the WaveHub site, where the WBA is applied – reveal that H_s and T_p parameters are most often estimated with a negative bias by Model 2, and the T_z estimate is overpredicted with a positive systematic bias, while the estimates from Model 1 are in relatively better alignment with the buoy data. Similar trends had already been identified in Section 4.2 in the comparison of the ship and buoy estimates at WaveHub, which suggests that the uncertainties in the input at WaveHub propagate into the output at Perranporth. On the contrary, at FabTest, which is the furthest validation point away from WaveHub, Model 1 and Model 2 have very similar error levels, so it seems like the output at FabTest is more influenced by the other two input points (Penzance and Looe Bay). Another important point to notice from the Q-Q plots in Figs. 15c and e is that the correlation between the T_E- and μ_P-quantiles from the buoy data, on the one hand, and the estimates from the surrogate models, on the other hand, is equally good for Models 1 and 2 at Perranporth. The greater discrepancy inferred from the error values reported in Table 4 for those two parameters can instead be attributed to more scattered estimates (i.e. *precision*, rather than *accuracy*) in the case of Model 2. To summarise the above results, it is demonstrated that, at all validation points, Model 2, which incorporates a WBA system, compares fairly well with Model 1, which uses only wave buoy data; some (limited) losses in accuracy and precision were identified for certain wave parameters.

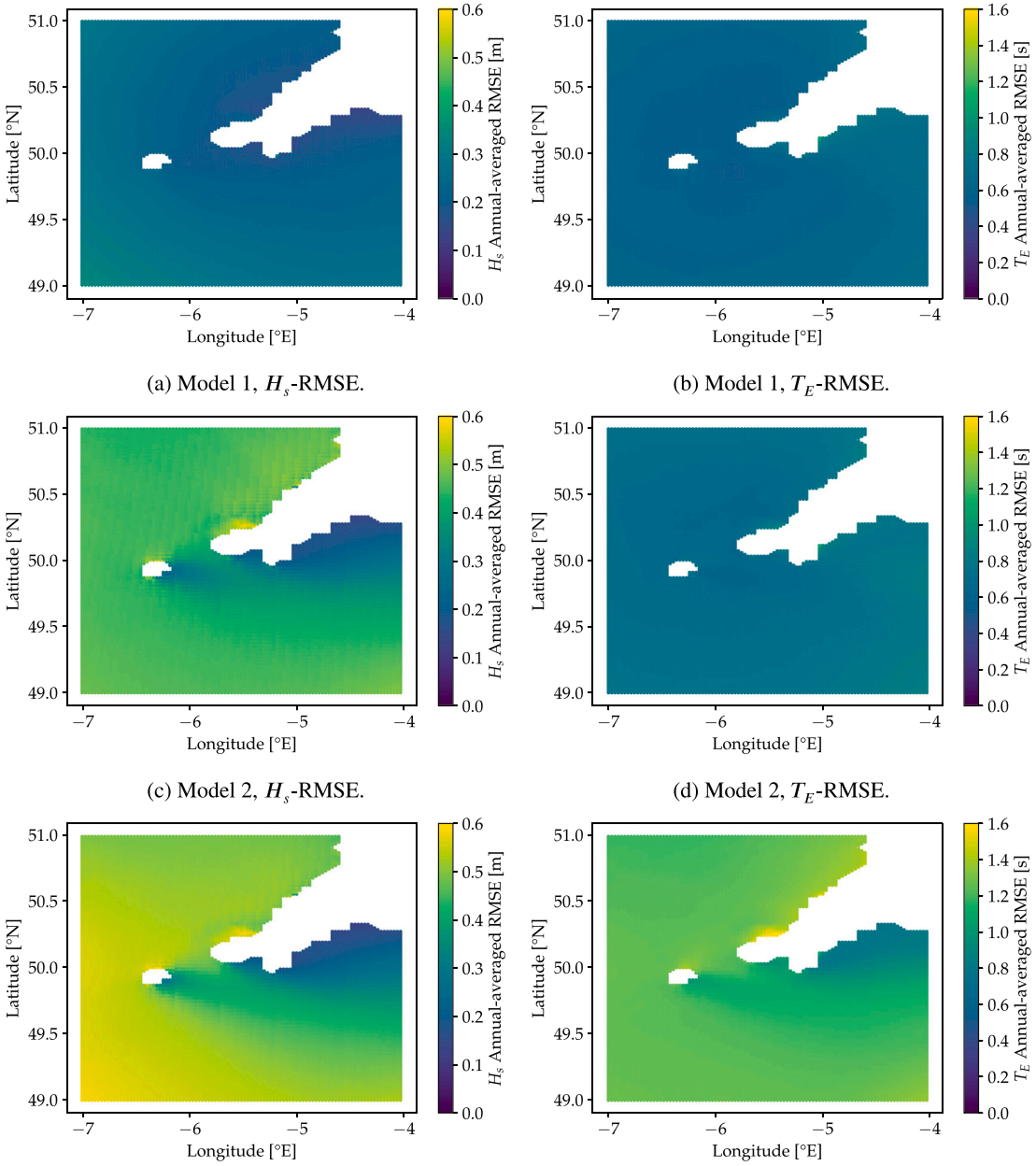

(a) Model 1, H_s-RMSE. (b) Model 1, T_E-RMSE.

(c) Model 2, H_s-RMSE. (d) Model 2, T_E-RMSE.

(e) Model 3, H_s-RMSE. (f) Model 3, T_E-RMSE.

Fig. 14. Surrogate model annual spatial difference between three surrogate models and UKMO model in terms of H_s and T_E estimation in 2016. Sub-figures (a), (c) and (e) are annual-averaged RMSE distribution for H_s estimation from Model 1, Model 2 and Model 3, respectively; Sub-figures (b), (d) and (f) are annual-averaged RMSE distribution for T_E estimation from the three models.

Focusing now on the performances of Model 3 with respect to those of Model 2, the error metrics have substantially larger values for the former (with a factor of 1.5–2.0 increase in the MAPE values for H_s, T_E, and T_p from Model 2 to Model 3) at Perranporth near the north coast of Cornwall, where Model 3 does not have any neighbouring observation input. In Fig. 15, the quantiles of estimates from Model 3 are those that deviate the most from the buoy data among all four models for all wave parameters, featuring remarkably irregular bias patterns. Comparatively, the Q-Q lines for Model 2 are more parallel to the lines of identity ($y = x$), showing more regular patterns. All this confirms the previous finding from Section 4.3 that the network with an incorporated WBA system at WaveHub performs better than the one having no measurement in that location. At Porthleven and FabTest, both located near the south coast of Cornwall close to the Penzance and Looe Bay inputs, the discrepancies in accuracy and precision between the surrogate models become insignificant.

Interestingly, from Table 4, the period estimates (T_E, T_z, T_p) by the three surrogate models tend to outperform the UKMO hindcast model at FabTest. At that location, the wave direction estimates from all four models have relatively large errors compared to the other two validation locations (with a factor of 2.0–2.9 increase in the RMSE of μ_P from Porthleven to FabTest sites). This could be caused by some weakness of the UKMO physics-based model to capture the wave properties at the specific location; however, a more detailed investigation would be needed to verify such a hypothesis and identify the real cause of the problem, which is out of the scope of the present paper. For now, it suffices to say that any dysfunction of the physics-based model at a grid point in the domain is likely to yield unavoidable deviations of the surrogate model outputs from the buoy data. These deviations are

Table 4
Model validation results. For each column, the best performances in terms of the highest R^2 values are highlighted in bold.

Model	Error metrics	Perranporth					Porthleven					FabTest				
		H_s	μ_p	T_E	T_z	T_p	H_s	μ_p	T_E	T_z	T_p	H_s	μ_p	T_E	T_z	T_p
Model 1 (3 buoys input)	RMSE	0.277	27.712	0.954	0.924	1.730	0.235	16.234	0.973	0.861	2.322	0.329	39.789	0.876	0.790	2.742
	MAE	0.198	13.994	0.638	0.709	1.104	0.163	11.711	0.671	0.622	1.613	0.235	24.391	0.688	0.613	1.984
	MAPE	0.172	N/A	0.077	0.120	0.115	0.164	N/A	0.084	0.115	0.169	0.342	N/A	0.113	0.160	0.393
	R^2	0.921	−0.056	0.789	**0.539**	**0.662**	0.912	−0.868	0.685	**0.528**	**0.393**	0.723	−0.717	0.301	**0.262**	0.100
Model 2 (2 buoys + vessel-as-a-buoy input)	RMSE	0.589	32.816	1.131	1.364	2.410	0.400	18.969	1.009	0.950	2.451	0.348	41.313	0.905	0.814	2.705
	MAE	0.375	20.645	0.787	1.182	1.699	0.251	15.071	0.703	0.740	1.758	0.239	25.182	0.715	0.633	1.989
	MAPE	0.254	N/A	0.097	0.216	0.160	0.247	N/A	0.090	0.145	0.180	0.350	N/A	0.117	0.167	0.390
	R^2	0.643	−0.216	0.702	−0.012	0.343	0.743	−0.975	0.662	0.425	0.323	0.690	−0.963	0.253	0.214	0.121
Model 3 (2 buoys input)	RMSE	0.656	27.766	1.879	1.422	2.724	0.293	19.303	1.205	1.056	2.436	0.323	40.518	0.815	0.829	2.694
	MAE	0.487	16.761	1.491	1.117	2.148	0.210	15.217	0.884	0.783	1.818	0.236	24.574	0.613	0.641	1.951
	MAPE	0.420	N/A	0.198	0.208	0.239	0.198	N/A	0.119	0.153	0.194	0.359	N/A	0.101	0.174	0.385
	R^2	0.557	−0.759	0.177	−0.100	0.161	0.862	−1.499	0.518	0.289	0.330	0.732	−0.753	**0.395**	0.184	**0.128**
Model 4 UKMO hindcast	RMSE	0.272	16.526	0.919	0.976	1.750	0.205	15.839	0.869	1.130	2.429	0.320	45.723	1.444	1.272	4.094
	MAE	0.205	10.425	0.677	0.694	1.097	0.145	10.678	0.619	0.767	1.489	0.216	29.116	1.033	0.856	2.689
	MAPE	0.175	N/A	0.085	0.115	0.124	0.140	N/A	0.078	0.139	0.166	0.291	N/A	0.172	0.221	0.555
	R^2	**0.923**	**0.252**	**0.805**	0.477	0.662	**0.934**	**−0.220**	**0.742**	0.192	0.324	**0.740**	**0.039**	−0.925	−0.894	−1.016

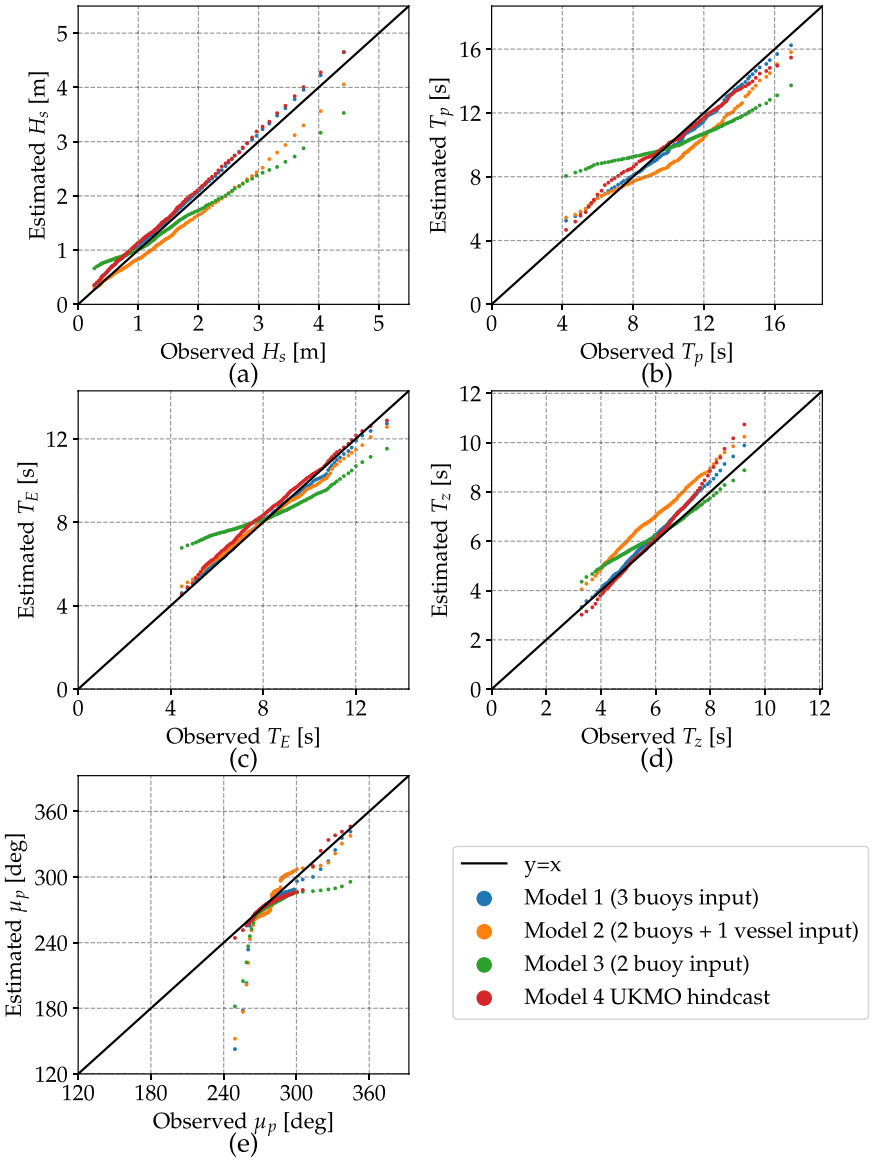

Fig. 15. Quantile–quantile (Q-Q) plot of the wave parameters between buoy observation (x-axes) and estimation (y-axes) by different models (Model 1, Model 2, Model 3 are surrogate spatial models with different inputs, Model 4 is the UKMO hindcast model) for Perranporth site in 2016: (a) Significant wave height H_s; (b) Peak period T_p; (c) Energy period T_E; (d) Zero-crossing period T_z; (e) Peak direction μ_p. The data corresponds to the 1st- to 99th-percentiles of the observations and model estimates.

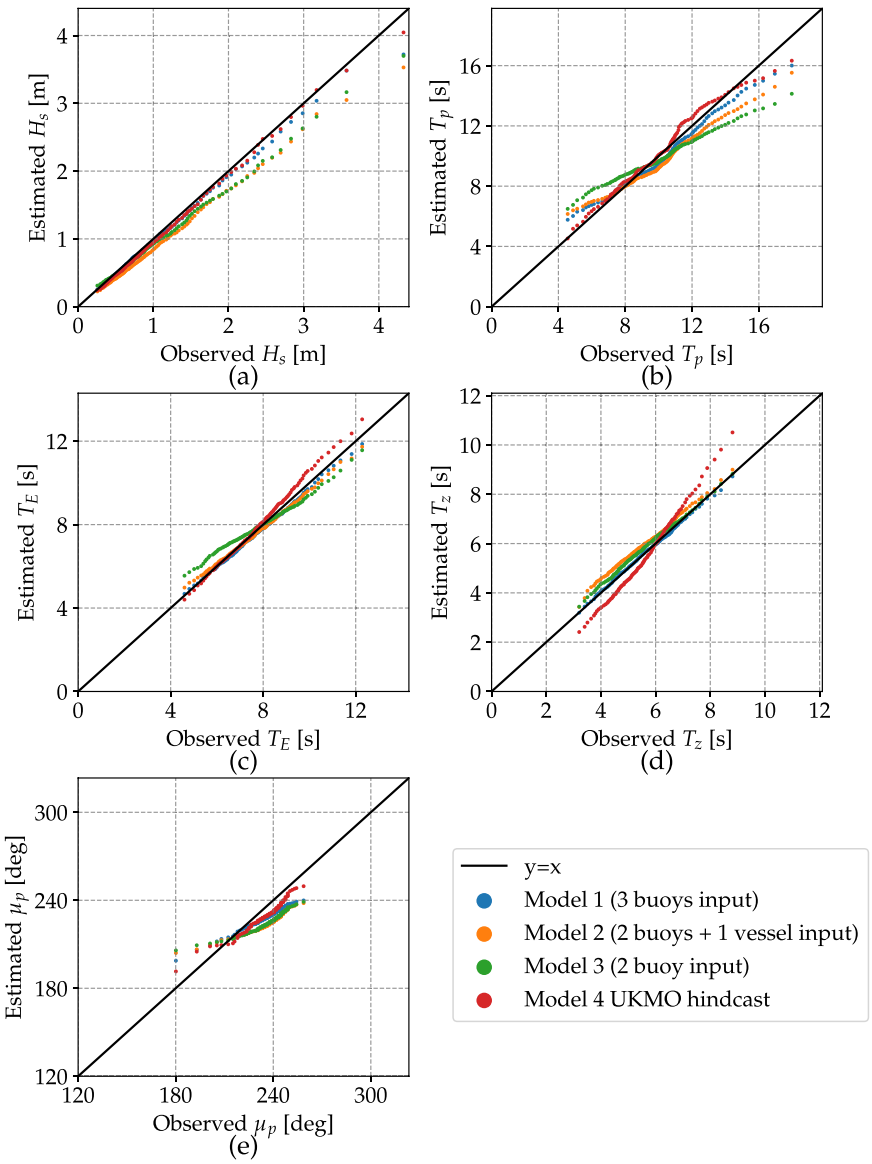

Fig. A.1. Q-Q plot of the wave parameters between buoy observation and estimation by different models for Porthleven site in 2016. More information in the caption of Fig. 15.

due to a lack of fidelity of the surrogate models to the (true) physical phenomena, inherited from the physics-based model during the training step. This is, for instance, what seems to be happening in Fig. 15e, where the UKMO model is not able to correctly capture the wave directions observed between 120° to 250°, and in consequence, the surrogate models all fail to accurately estimate the directions in this range as well.

4.5. Further discussion on the limitations of the proposed wave observation network

The study emphasised the main complications inherent to the wave-buoy analogy in connection with Model 2, especially the wave-filtering effect that tends to underestimate the energy levels in the wave spectrum, yielding negative biases in the estimated values of H_s, as well as positive biases in the T_{m01} and T_z parameters. To mitigate this effect, the correction of the ship-based estimates could be made possible by, for example combining the ship-as-a-wave-buoy results with estimates from other shipborne instruments such as wave radars. This idea could be further explored and adapted for use with the surrogate model.

The present work disregarded any uncertainty in the vessel model, using the same set of first-order transfer functions for simulating the wave-induced motions as for producing sea state estimates. In practice, the latter procedure will be impacted by various sources of uncertainties, especially possible higher-order nonlinear effects and data inaccuracies – due to e.g. sensor malfunction, misalignment of the axes, bias, misplacement[6], noise, etc. – which will appear in the measured ship motions but cannot be captured by the theoretical calculations in the SSE algorithm. This motivates extended studies dedicated to the incorporation of actual measurements from several in-service vessels in the established framework. Real-time wave estimation based on such observations within large-scale geographical areas could be investigated over spatial domains that extend further away from the shore, even where buoy data become scarcer, with the aim to provide complementary hindcast and forecast datasets. Refinements of the method – e.g. by means of a benchmark against various surrogate model architectures, different input/output parameter sets, and other machine learning algorithms – are expected to help improve the overall

[6] The inertial sensor is never mounted exactly at the centre of gravity. In fact, the ideal placement would be at the centres of rotation of both roll and pitch motions, which in practice for a ship are not located at a single point.

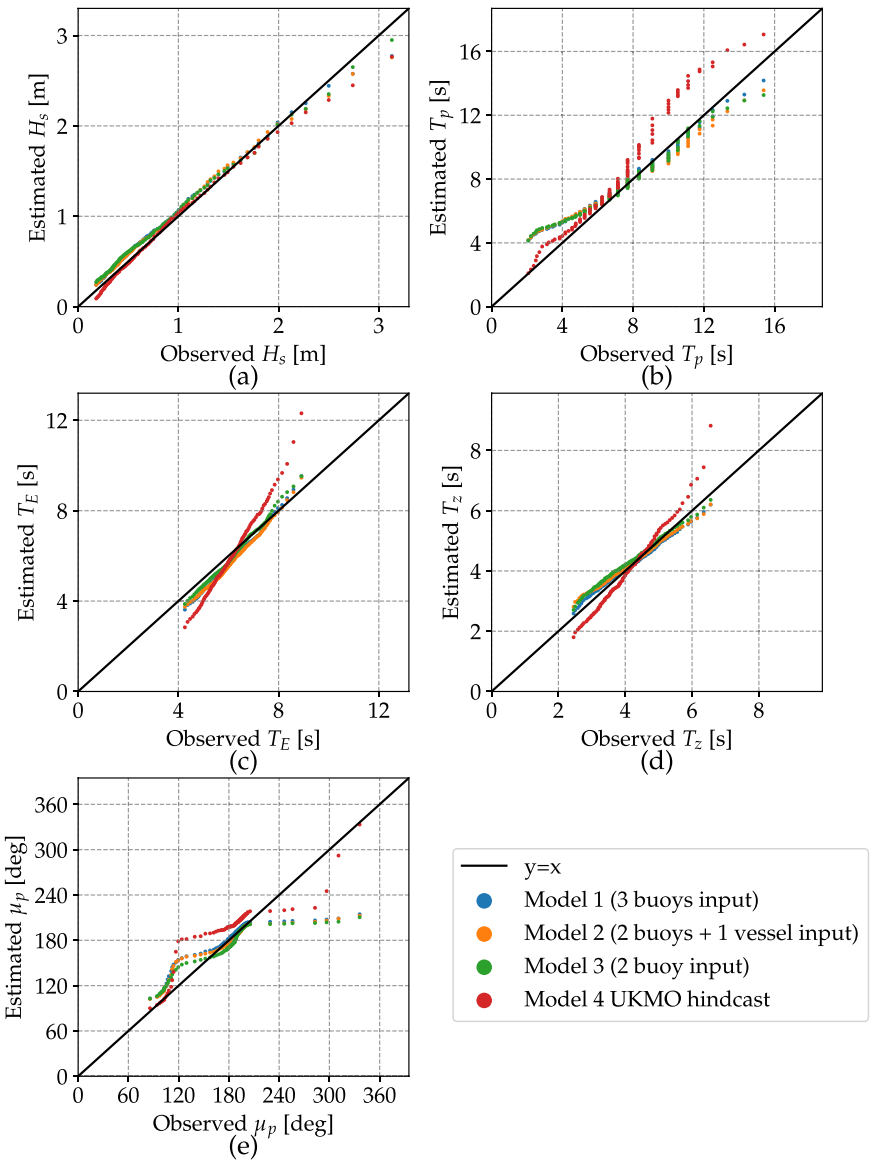

Fig. A.2. Q-Q plot of the wave parameters between buoy observation and estimation by different models for FabTest site in 2016. More information in the caption of Fig. 15.

performance, and especially needed when more vessel-based estimates are incorporated.

As a final remark, the scope was limited to the analysis of the nowcasting performance of a hybrid ship–buoy wave observation network. Nonetheless, the ultimate goal of the project is the forecast of offshore and near-shore wave conditions ahead of time. Research was initiated in this direction, with interesting results in Chen et al. (2022). One could imagine in the near future the possibility to deploy a fleet of small autonomous vessels in the area of interest to collect spatial wave data, to be used for wave predictions in the planning of offshore operations, with the goal of better evaluating the weather-related risks for people and structures.

5. Conclusions

In this paper, the authors have proposed the use of direct wave measurement from vessels as inputs to an existing surrogate wave modelling framework in order to derive spatial wave data across a whole regional domain from a network of buoys and ships.

The method relies on a machine learning model that learns the spatial correlations of ocean wave parameters between grid points from a wave hindcast database. Once trained, the model acts as a surrogate of the physics-based model and a very limited number of triplet point observations suffices to estimate the sea state parameters at all grid points with similar accuracy. Ship response-based estimates are incorporated into the observational network and results show promising nowcasting capabilities in substituting buoy records with available vessel-based data. In particular, the main findings are highlighted here:

- The output sea state estimates from a WBA sensor system can be integrated into a broader surrogate modelling system that combines input from buoys and ships;
- Integrating a vessel within the observation network at a location where buoy data is missing improves the accuracy and precision of the output spatial wave data over a large extent of the computational domain;
- The hybrid ship–buoy observation system can provide accuracy similar to an advanced nearshore wave modelling system, with a fraction of the computational cost;
- The system has significant potential for expansion into a network of available vessels to further improve the reliability and availability of wave data, especially in locations where the more traditional observation platforms are scarce.

CRediT authorship contribution statement

Raphaël E.G. Mounet: Conceptualization, Methodology, Software, Validation, Formal analysis, Visualization, Writing – original draft. **Jiaxin Chen:** Conceptualization, Methodology, Software, Validation, Formal analysis, Visualization, Writing – original draft. **Ulrik D. Nielsen:** Conceptualization, Methodology, Writing – review & editing, Supervision, Funding acquisition. **Astrid H. Brodtkorb:** Conceptualization, Methodology, Writing – review & editing, Supervision, Funding acquisition. **Ajit C. Pillai:** Conceptualization, Methodology, Resources, Data curation, writing – review & editing, supervision, funding acquisition. **Ian G.C. Ashton:** Resources, Data curation, Writing – review & editing, Supervision, Funding acquisition. **Edward C.C. Steele:** Resources, Data curation, Writing – review & editing.

Declaration of competing interest

The authors declare that they have no known competing financial interests or personal relationships that could have appeared to influence the work reported in this paper.

Data availability

Links to the data that has been used are provided in the paper.

Acknowledgements

Source data in the preparation of this paper has been supplied by the Channel Coastal Observatory, UK, funded under the regional coastal monitoring programmes by DEFRA. This work was supported by the Research Council of Norway through the Centres of Excellence funding scheme [project number 223254 AMOS]; the Danish Maritime Fund [case numbers 2017–101 and 2020–074]; and the EPSRC Supergen Offshore Renewable Energy Hub (http://doi.org/10.13039/501100000266) [grant number EP/S000747/1] Flexible Fund support for MalCOM. A.C. Pillai acknowledges support from the Royal Academy of Engineering under the Research Fellowship scheme (award number: RF\202021\20\175).

Appendix. Complementary validation results

Additional Q-Q plots are given in Figs. A.1 and A.2 showing the correlation between the model outputs and the buoy observations at Porthleven and FabTest, respectively.

References

Alvarez Fanjul, E., Ciliberti, S.A., Bahurel, P. (Eds.), 2022. Implementing Operational Ocean Monitoring and Forecasting Systems, first ed. In: GOOS-275, IOC-UNESCO, Paris, France, http://dx.doi.org/10.25607/OBP-1774.

Anderson, G., Carse, F., Turton, J., Saulter, A., 2016. Quantification of bias of wave measurements from lightvessels. J. Oper. Oceanogr. 9 (2), 93–102. http://dx.doi.org/10.1080/1755876X.2016.1239242.

Ashton, I.G.C., Johanning, L., 2014. Wave energy testing in Cornwall: Were the waves during winter 2013/14 exceptional? In: Int. Conf. Offshore Renew. Energy. ASRANet.

Bendat, J.S., Piersol, A.G., 2011. Random Data: Analysis and Measurement Procedures, fourth ed. John Wiley & Sons.

Benoit, M., Frigaard, P., Schäffer, H.A., 1997. Analysing multidirectional wave spectra: a tentative classification of available methods. In: Proc. 27th IAHR Congress, San Francisco, 10-15 August 1997. National Res. Council of Canada, pp. 131–158.

Booij, N., Ris, R.C., Holthuijsen, L.H., 1999. A third-generation wave model for coastal regions: 1. Model description and validation. J. Geophys. Res. 104 (C4), 7649–7666. http://dx.doi.org/10.1029/98JC02622.

Brandt, A., 2011. Noise and Vibration Analysis: Signal Analysis and Experimental Procedures. John Wiley & Sons, http://dx.doi.org/10.1002/9780470978160.

Breiman, L., 2001. Random forests. Mach. Learn. 45 (1), 5–32.

Brodtkorb, A.H., Nielsen, U.D., 2022. Automatic sea state estimation with online trust measure based on ship response measurements. Control Eng. Pract. 130, 105375. http://dx.doi.org/10.1016/j.conengprac.2022.105375.

Brodtkorb, A.H., Nielsen, U.D., J. Sørensen, A., 2018b. Sea state estimation using vessel response in dynamic positioning. Appl. Ocean Res. 70, 76–86. http://dx.doi.org/10.1016/j.apor.2017.09.005.

Brodtkorb, A.H., Nielsen, U.D., Sørensen, A., 2018a. Online wave estimation using vessel motion measurements. IFAC-PapersOnLine 51 (29), 244–249. http://dx.doi.org/10.1016/j.ifacol.2018.09.510.

Browne, M., Castelle, B., Strauss, D., Tomlinson, R., Blumenstein, M., Lane, C., 2007. Near-shore swell estimation from a global wind-wave model: Spectral process, linear, and artificial neural network models. Coast. Eng. 54 (5), 445–460. http://dx.doi.org/10.1016/j.coastaleng.2006.11.007.

Chen, J., Ashton, I.G., Steele, E.C., Pillai, A.C., 2022. A real-time spatio-temporal machine learning framework for the prediction of nearshore wave conditions. Artif. Intell. Earth Syst. 1–51. http://dx.doi.org/10.1175/AIES-D-22-0033.1.

Chen, X., Okada, T., Kawamura, Y., Mitsuyuki, T., 2020. Estimation of on-site directional wave spectra using measured hull stresses on 14,000 TEU large container ships. J. Mar. Sci. Technol. 25 (3), 690–706. http://dx.doi.org/10.1007/s00773-019-00673-w.

Chen, J., Pillai, A.C., Johanning, L., Ashton, I., 2021. Using machine learning to derive spatial wave data: A case study for a marine energy site. Environ. Model. Softw. 142, 105066. http://dx.doi.org/10.1016/j.envsoft.2021.105066.

Datawell, 2020. Datawell Waverider Reference Manual. Technical Report, Datawell BV oceanographic instruments, 1704 RP Heerhugowaard, The Netherlands, URL: www.datawell.nl.

DNV, 2010. Recommended Practice DNV-RP-C205: Environmental Conditions and Environmental Loads. Det Norske Veritas, Oslo, Norway.

Fathi, D.E., 2018. ShipX Vessel Responses (VERES), User's Manual. Technical Report, SINTEF Ocean A/S.

Graham, J.A., O'Dea, E., Holt, J., Polton, J., Hewitt, H.T., Furner, R., Guihou, K., Brereton, A., Arnold, A., Wakelin, S., et al., 2018. AMM15: a new high-resolution NEMO configuration for operational simulation of the European north-west shelf. Geosci. Model Dev. 11 (2), 681–696.

Günther, H., Hasselmann, S., Janssen, P.A., 1992. The WAM Model Cycle 4. Technical Report, Deutsches Klimarechenzentrum (DKRZ).

Hashimoto, N., 1997. Analysis of the directional wave spectrum from field data. Adv. Coast. Ocean Eng. 3, 103–144.

Hastie, T., Tibshirani, R., Friedman, J.H., Friedman, J.H., 2009. The Elements of Statistical Learning: Data Mining, Inference, and Prediction, Vol. 2. Springer.

Hauser, D., Kahma, K., Krogstad, H.E., Lehner, S., Monbaliu, J.A.J., Wyatt, L.R., 2005. Measuring and analysing the directional spectra of ocean waves. EU COST Action 714.

Iseki, T., Ohtsu, K., 2000. Bayesian estimation of directional wave spectra based on ship motions. Control Eng. Pract. 8 (2), 215–219. http://dx.doi.org/10.1016/S0967-0661(99)00156-2.

James, S.C., Zhang, Y., O'Donncha, F., 2018. A machine learning framework to forecast wave conditions. Coast. Eng. 137, 1–10. http://dx.doi.org/10.1016/j.coastaleng.2018.03.004.

Kim, T., Lin, L.-H., Wang, H., 1995. Application of maximum entropy method to the real sea data. In: Proc. 24th Int. Conf. Coast. Eng. 1994. pp. 340–355. http://dx.doi.org/10.1061/9780784400890.027.

Kobune, K., Hashimoto, N., 1986. Estimation of directional spectra from the maximum entropy principle. In: Int. Offshore Mech. Arc. Eng. Symp. Vol. 5. pp. 80–85.

Komen, G.J., Cavaleri, L., Donelan, M., Hasselmann, K., Hasselmann, S., Janssen, P. (Eds.), 1996. Dynamics and Modelling of Ocean Waves. Cambridge University Press, Cambridge, UK, p. 554.

Krogstad, H.E., Wolf, J., Thompson, S.P., Wyatt, L.R., 1999. Methods for intercomparison of wave measurements. Coast. Eng. 37 (3–4), 235–257. http://dx.doi.org/10.1016/S0378-3839(99)00028-9.

Lavidas, G., Venugopal, V., Friedrich, D., 2017. Sensitivity of a numerical wave model on wind re-analysis datasets. Dyn. Atmos. Oceans 77, 1–16. http://dx.doi.org/10.1016/j.dynatmoce.2016.10.007.

Mittendorf, M., Nielsen, U.D., Bingham, H.B., Storhaug, G., 2022. Sea state identification using machine learning: A comparative study based on in-service data from a container vessel. Mar. Struct. 85, 103274. http://dx.doi.org/10.1016/j.marstruc.2022.103274.

Mounet, R.E.G., Nielsen, U.D., Brodtkorb, A.H., Tannuri, E.A., de Mello, P.C., 2022. Simultaneous sea state estimation and transfer function tuning using a network of dynamically positioned ships. Appl. Ocean Res. 129, 103367. http://dx.doi.org/10.1016/j.apor.2022.103367.

Nielsen, U., 2006. Estimations of on-site directional wave spectra from measured ship responses. Mar. Struct. 19 (1), 33–69. http://dx.doi.org/10.1016/j.marstruc.2006.06.001.

Nielsen, U.D., 2007. Response-based estimation of sea state parameters – Influence of filtering. Ocean Eng. 34 (13), 1797–1810. http://dx.doi.org/10.1016/j.oceaneng.2007.03.002.

Nielsen, U.D., 2017. A concise account of techniques available for shipboard sea state estimation. Ocean Eng. 129, 352–362. http://dx.doi.org/10.1016/j.oceaneng.2016.11.035.

Nielsen, U.D., H. Brodtkorb, A., J. Sørensen, A., 2019. Sea state estimation using multiple ships simultaneously as sailing wave buoys. Appl. Ocean Res. 83, 65–76. http://dx.doi.org/10.1016/j.apor.2018.12.004.

Nielsen, U.D., Stredulinsky, D.C., 2012. Sea state estimation from an advancing ship – A comparative study using sea trial data. Appl. Ocean Res. 34, 33–44. http://dx.doi.org/10.1016/j.apor.2011.11.001.

van Nieuwkoop, J.C., Smith, H.C., Smith, G.H., Johanning, L., 2013. Wave resource assessment along the cornish coast (UK) from a 23-year hindcast dataset validated against buoy measurements. Renew. Energy 58, 1–14.

Pascoal, R., Guedes Soares, C., 2009. Kalman filtering of vessel motions for ocean wave directional spectrum estimation. Ocean Eng. 36 (6–7), 477–488. http://dx.doi.org/10.1016/j.oceaneng.2009.01.013.

Portilla, J., Ocampo-Torres, F.J., Monbaliu, J., 2009. Spectral partitioning and identification of wind sea and swell. J. Atmos. Ocean. Technol. 26 (1), 107–122. http://dx.doi.org/10.1175/2008JTECHO609.1.

Ris, R., Holthuijsen, L., Booij, N., 1999. A third-generation wave model for coastal regions: 2. Verification. J. Geophys. Res. 104 (C4), 7667–7681. http://dx.doi.org/10.1029/1998JC900123.

Saulter, A., 2021. Quality Information Document for the CMEMS North West European Shelf Wave Hindcast, CMEMS-NWS-QUID-004-015. Technical Report, Copernicus Marine Service.

de Souza, F.L., Tannuri, E.A., de Mello, P.C., Franzini, G., Mas-Soler, J., Simos, A.N., 2017. Bayesian estimation of directional wave-spectrum using vessel movements and wave-probes: Proposal and preliminary experimental validation. In: Proc. Int. Conf. Offshore Mech. Arct. Eng. (OMAE'17). American Society of Mechanical Engineers (ASME), http://dx.doi.org/10.1115/OMAE2017-61241.

Tannuri, E.A., Sparano, J.V., Simos, A.N., Da Cruz, J.J., 2003. Estimating directional wave spectrum based on stationary ship motion measurements. Appl. Ocean Res. 25 (5), 243–261. http://dx.doi.org/10.1016/j.apor.2004.01.003.

Tolman, H.L., Balasubramaniyan, B., Burroughs, L.D., Chalikov, D.V., Chao, Y.Y., Chen, H.S., Gerald, V.M., 2002. Development and implementation of wind-generated ocean surface wave models at NCEP. Weather Forecast. 17 (2), 311–333.

Tolman, H.L., et al., 2009. User Manual and System Documentation of WAVEWATCH III TM Version 3.14. Technical Note, MMAB Contribution.

Tucker, M.J., Pitt, E.G., 2001. Waves in Ocean Engineering, Vol. 5. Elsevier Ocean Engineering Book Series.

Virtanen, P., Gommers, R., Oliphant, T.E., Haberland, M., Reddy, T., Cournapeau, D., Burovski, E., Peterson, P., Weckesser, W., Bright, J., van der Walt, S.J., Brett, M., Wilson, J., Millman, K.J., Mayorov, N., Nelson, A.R.J., Jones, E., Kern, R., Larson, E., Carey, C.J., Polat, İ., Feng, Y., Moore, E.W., VanderPlas, J., Laxalde, D., Perktold, J., Cimrman, R., Henriksen, I., Quintero, E.A., Harris, C.R., Archibald, A.M., Ribeiro, A.H., Pedregosa, F., van Mulbregt, P., SciPy 1.0 Contributors, 2020. SciPy 1.0: Fundamental algorithms for scientific computing in python. Nature Methods 17, 261–272. http://dx.doi.org/10.1038/s41592-019-0686-2.

Welch, P., 1967. The use of fast Fourier transform for the estimation of power spectra: A method based on time averaging over short, modified periodograms. IEEE Trans. Audio Electroacoust. 15 (2), 70–73. http://dx.doi.org/10.1109/TAU.1967.1161901.

Wilks, D.S., 2011. Statistical Methods in the Atmospheric Sciences, Vol. 100. Academic Press.

Zago, L., Simos, A.N., Kawano, A., Kogishi, A.M., 2023. A new vessel motion based method for parametric estimation of the waves encountered by the ship in a seaway. Appl. Ocean Res. 134, 103499. http://dx.doi.org/10.1016/j.apor.2023.103499.